Exploring fingerprints of ultrafast structural dynamics in molecular solutions with an x-ray laser

PCCP

Exploring fingerprints of ultrafast structural dynamics in molecular solutions with an x-ray laser[†]

Ruslan P. Kurta,[*a] Tim B. van Driel,[b] Asmus O. Dohn,[c,d] Tim B. Berberich,[a] Silke Nelson,[b] Ivan A. Zaluzhnyy,[e‡] Nastasia Mukharamova,[f] Dmitry Lapkin,[f‡] Diana B. Zederkof,[c¶] Matt Seaberg,[b] Kasper S. Pedersen,[g] Kasper S. Kjær,[h] Geoffery Ian Rippy,[k] Elisa Biasin,[h#] Klaus B. Møller,[g] Luca Gelisio,[f¶] Kristoffer Haldrup,[c] Ivan A. Vartanyants,[f] and Martin M. Nielsen [*c]

We apply ultrashort x-ray laser pulses to track optically excited structural dynamics of $[Ir_2(dimen)_4]^{2+}$ molecules in solution. In our exploratory study we determine angular correlations in the scattered x-rays, which comprise a complex fingerprint of the ultrafast dynamics. Model-assisted analysis of the experimental correlation data allows us to elucidate various aspects of the photoinduced changes in the excited molecular ensembles. We unambiguously identify that in our experiment the photoinduced transition dipole moments in $[Ir_2(dimen)_4]^{2+}$ molecules are oriented perpendicular to the Ir-Ir bond. The analysis also shows that the ground state conformer of $[Ir_2(dimen)_4]^{2+}$ with a larger Ir–Ir distance is mostly responsible for the formation of the excited state. We also reveal that the ensemble of solute molecules can be characterized with a substantial structural heterogeneity due to solvent influence. The proposed x-ray correlation approach offers an alternative path for studies of ultrafast structural dynamics of molecular ensembles in the liquid and gas phases.

1 Introduction

Ultrafast dynamics of photoexcited molecules in solution involves processes at a range of length and time scales, such as charge

[a] European XFEL, Holzkoppel 4, D-22869 Schenefeld, Germany. E-mail: ruslan.kurta@xfel.eu
[b] SLAC National Accelerator Laboratory, 2575 Sand Hill Road, Menlo Park, CA 94025, USA
[c] Department of Physics, Technical University of Denmark, Fysikvej 307, DK-2800 Lyngby, Denmark. E-mail: mmee@fysik.dtu.dk
[d] Science Institute and Faculty of Physical Sciences, University of Iceland VR-III, 107 Reykjavík, Iceland
[e] Department of Physics, University of California San Diego, 9500 Gilman Dr, La Jolla, CA 92093, USA
[f] Deutsches Elektronen-Synchrotron DESY, Notkestraße 85, D-22607 Hamburg, Germany
[g] Department of Chemistry, Technical University of Denmark, Fysikvej 307, DK-2800 Lyngby, Denmark
[h] Stanford PULSE Institute, SLAC National Accelerator Laboratory, Stanford University, Menlo Park, CA 94025, USA
[k] Department of Materials Science and Engineering, University of California Davis, 1 Shields Ave, Davis, CA 95616, USA
[*] Corresponding authors
[†] Electronic Supplementary Information (ESI) available. See DOI: 10.1039/cXCP00000x/
[‡] Present address: Institute of Applied Physics, University of Tübingen, Auf der Morgenstelle 10, D-72076 Tübingen, Germany
[¶] Present address: European XFEL, Holzkoppel 4, D-22869 Schenefeld, Germany
[#] Present address: Pacific Northwestern National Laboratory, Richland, WA 99352, USA

and spin rearrangements, changes in the atomic structure of the solute molecules and solvation shell, or coherent vibrations of molecules [1–7]. It is not surprising that direct identification of different aspects of such multifold dynamics in a single experiment is challenging due to complex interplay of different structural and energetic factors [8]. As a result, the time-energy landscape of chemical reactions has been traditionally in the focus of spectroscopy studies, while scattering is typically used to probe the structure [9–22]. The emergence of ultrabright hard x-ray free-electron laser (XFEL) sources opened exciting possibilities for time-resolved x-ray studies [23–28]. The intense and ultrashort x-ray pulses produced by XFELs allow one to access high-resolution structural information from solution scattering at femtosecond and picosecond timescales [29–35], as recently reviewed by e.g. Choi et al. [36].

It was first realized in ultrafast electron diffraction studies of gas-phase molecules [37–41], that the structural information of diffuse scattering measurements can be enhanced by applying a linearly polarized optical laser pump. In such a case, preferential excitation of molecules with specific orientations leads to angular anisotropic diffuse scattering [42–44]. The ability to detect and separate the isotropic and anisotropic scattering contributions allows one to advance in diffuse scattering data interpretation [41]. A similar approach has been also employed in the x-ray domain [39,45,46], particularly in the time-resolved x-ray solution scattering (TRXSS) [47,48]. It is also common to apply Legendre polynomial expansion of the TRXSS signal measured on a two-dimensional (2D) detector, where the expansion coefficients can be directly related to the isotropic $\Delta S_0(q)$ and anisotropic $\Delta S_2(q)$ contributions to TRXSS [45,47,49]. Such decomposition into $\Delta S_0(q)$ and $\Delta S_2(q)$ components can provide higher fidelity in the analysis by more clearly disentangling solute and solvent contributions to the difference signals [47,48].

In this work we employ the angular cross-correlation functions [50–52], which provide an alternative way for analysis of TRXSS measurements. This approach is general and can be used to study dynamics in the liquid or gas phase, by applying either ultrafast electron or x-ray scattering. The idea to use angular correlations in the structural studies of particle solutions by means of x-ray scattering was initially proposed to facilitate biological structure determination [53], and has been recently experimentally realized with an XFEL [54,55]. In this type of studies, one relies on a uniform distribution of orientations of illuminated particles. At the same time, the angular cross-correlation functions (CCFs) have been also employed to characterize the structure of partially aligned systems, such as hexatic liquid crystals [56,57], nanoparticle solutions [58], or self-assembled lipids [59]. The first application of the CCF analysis in the pump-probe solution experiments on solvated $[Pt_2(P_2O_5H_2)_4]^{4-}$ molecules with an XFEL demonstrated its potential to extract information on the structural dynamics, similar to a more established TRXSS approach [60]. In the present work, we expand on these initial efforts by applying the CCF analysis in combination with hybrid Quantum Mechanical/Molecular Mechanical Born–Oppenheimer Molecular Dynamics (QM/MM BOMD) modeling of structural dynamics following photoexcitation of $[Ir_2(dimen)_4]^{2+}$ (dimen=1,8-diisocyano-

p-menthane) complexes [61] [see Fig. 1]. We determined angular correlations of x-rays scattered from $[Ir_2(dimen)_4]^{2+}$ solutions in an optical pump – x-ray probe experiment with an XFEL. Model-assisted Fourier analysis of the angular CCFs was employed for interpretation of the experimental correlation data.

2 Photochemistry of $[Ir_2(dimen)_4]^{2+}$

The $[Ir_2(dimen)_4]^{2+}$ molecule belongs to a class of $d^8 - d^8$ dimeric complexes with interesting photophysical properties as recently reviewed by Gray et al. [62]. Optical spectroscopy and x-ray diffraction investigations of $[Ir_2(dimen)_4]^{2+}$ have demonstrated that the ground state (GS) population exhibits structural isomerism with the two isomer populations equally populated at room temperature and varying in their Ir–Ir distance d_{Ir-Ir}, with the "long/eclipsed" (GS_{LG}) conformers having $d_{Ir-Ir} = 4.3$ Å and the "short/twisted" (GS_{SH}) conformers having $d_{Ir-Ir} = 3.6$ Å and exhibiting a dihedrally twisted structure [63–65].

The absorption spectrum of $[Ir_2(dimen)_4]^{2+}$ indicates distinct excitation pathways in the ultraviolet-visible (UV-Vis) spectral range [66]. Upon photo-excitation in the visible region (450-650 nm), an electron is promoted from the antibonding highest occupied molecular orbital (HOMO) $d\sigma^*$ to the lowest unoccupied molecular orbital (LUMO) $p\sigma$, and as the latter has bonding character and is located between the two Ir atoms this excitation leads to a pronounced contraction along the Ir-Ir axis, with the excited state exhibiting an Ir–Ir distance of $d_{Ir-Ir} = 2.92$ Å accompanied with a dihedral twist of around 15 degrees [64,67] (see Fig. 1). In the UV range (300-400 nm) the absorption spectrum of $[Ir_2(dimen)_4]^{2+}$ features two relatively narrow UV bands centered at 316 nm and 375 nm, which are formed by predominantly $^1d\pi \rightarrow p\sigma$ and $^3d\pi \rightarrow p\sigma$ excitations, respectively [66]. The Ir-Ir bond distances are expected to decrease in the $d\pi p\sigma$ excited states, although less than in the case of $d\sigma^* p\sigma$ state. Different strength of the Ir-Ir bond in the two GS conformers allows for preferential excitation of the "long" and "short" conformers in the visible region within the bands centered at 480 nm and 590 nm, respectively [66]. In the UV range both conformers absorb at virtually identical wavelengths, therefore it is impossible to achieve such selectivity by tuning the optical wavelength.

The electronic excitations in the visible range have been shown to exhibit a well-defined transition dipole moment (TDM) along the Ir-Ir axis [68]. As discussed in reference [67] excitation with a linearly polarized laser pulse leads to an excitation probability proportional to $\cos^2 \Psi$, where Ψ is the angle between the TDM of the molecule and the polarization direction of the optical laser pulse. This, in turn, leads to a rotationally anisotropic distribution of photo-excited molecules.

3 Experiment

The optical pump – x-ray probe experiment [see Fig. 2] was carried out at the X-ray Correlation Spectroscopy (XCS) instrument at the Linac Coherent Light Source (LCLS) XFEL facility [69]. A 6 mM sample solution of $[Ir_2(dimen)_4]^{2+}$ in acetonitrile was delivered to the interaction point in a liquid jet of about 50 μm in diameter. The sample was excited with 398 nm optical laser pulses of 40 fs duration and pulse energy of 5 μJ, focused onto
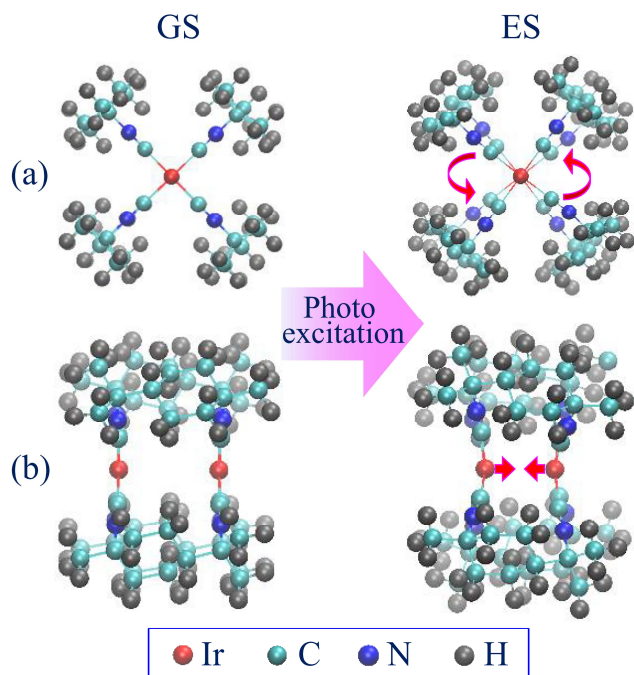
Fig. 1 A sketch of intramolecular structural changes in $[\text{Ir}_2(\text{dimen})_4]^{2+}$ upon photoexcitation. Two orthogonal views of the molecule in the GS (long conformer) and ES states are shown, with the Ir-Ir axis oriented perpendicular (a) and parallel (b) to the sheet plane. The optical excitation leads to contraction of the Ir-Ir bond, as well as N-Ir-Ir-N dihedral angle twist in the ES structure (schematically denoted with arrows).

a spot of 150 μm (FWHM). X-ray scattering was produced by 9.5 keV x-ray pulses of duration of 40 fs, focused to a spot of 20 μm (FWHM). The scattered signal was measured in the forward scattering geometry with a large-area hybrid pixel detector ePix10K (2.16 Megapixel, pixel size of 100 μm $\times$ 100 μm) developed at SLAC[70]. The detector was placed at a distance of 56 mm downstream from the interaction point, and was recording the scattering data at the repetition rate of 120 Hz. In our experiment horizontally polarized x-rays were applied, while the polarization direction of the optical pulses was tilted by 20° of the vertical direction. The optical pump and x-ray probe pulses were adjusted to achieve positional overlap at the same sample interaction point. A single pump-probe measurement provides a scattering image of the sample at a time delay t between the pump and probe pulses. Absolute time zero ($t = 0$) was determined from the optical Kerr response of the solvent to the optical excitation as the difference scattering signal from this effect exhibits a sub-100 fs rise time[32,71]. During sample measurements the time delay stage was continuously scanned to assure a uniform sampling of delay times t in the desired range. The XCS timing tool allowed us to accurately determine the time delays t in the range from -0.5 to

2.5 ps and achieve a sub-100 fs temporal resolution. A data preprocessing protocol involving data filtering and correcting (see section S1 of the ESI†) has been applied before computing the CCFs.

4 Fourier analysis of the angular cross-correlation functions

We applied angular CCFs and their Fourier components to analyze ultrafast structural dynamics captured in the scattering patterns. To detect structural changes in the sample at specific time delay t after applying an optical trigger it is common to operate with difference images,

$$I_{\text{diff}}(q, \varphi, t) = I_{\text{on}}(q, \varphi, t) - I_{\text{off}}(q, \varphi), \tag{1}$$

where $I_{\text{on}}(q, \varphi, t)$ is measured from the pumped sample at time delay t, and $I_{\text{off}}(q, \varphi)$ is measured from the unpumped sample in the ground state. It is expected that $I_{\text{on}}(q, \varphi, t < 0) \equiv I_{\text{off}}(q, \varphi)$ for a properly calibrated experimental time zero ($t = 0$). In Eq. (1) we consider diffraction patterns in the polar coordinate system $\mathbf{q} = (q, \varphi)$ defined in the detector plane (x, y) [see Fig. 2(a)]. We define the time-resolved angular cross-correlation function (CCF) $C_{\text{diff}}(q_1, q_2, \Delta, t)$ at delay time t for a difference image $I_{\text{diff}}(q, \varphi, t)$ as

$$C_{\text{diff}}(q_1, q_2, \Delta, t) = \langle I_{\text{diff}}(q_1, \varphi, t) I_{\text{diff}}(q_2, \varphi + \Delta, t) \rangle_{\varphi}, \tag{2}$$

where $q_1 = |\mathbf{q_1}|$, $q_2 = |\mathbf{q_2}|$, and the angles Δ and φ are determined in the range $[0, 2\pi)$ [see Fig. 2(a)]. Here the averaging $\langle \rangle_{\varphi}$ is performed over the angular coordinate φ, that is $\langle I_{\text{diff}}(q, \varphi, t) \rangle_{\varphi} \equiv I_{\text{diff}}(q, t) = 1/(2\pi) \int_0^{2\pi} I_{\text{diff}}(q, \varphi, t) d\varphi$.

We then determine the Fourier components (FCs) of the CCF (2) as,

$$C_{\text{diff}}^n(q_1, q_2, t) = \frac{1}{2\pi} \int_0^{2\pi} C_{\text{diff}}(q_1, q_2, \Delta, t) \exp(-in\Delta) d\Delta, \tag{3}$$

where n is the order of the FC $C_{\text{diff}}^n(q_1, q_2, t)$.

One can show that FCs $C_{\text{diff}}^n(q_1, q_2, t)$ can be generally represented as a sum of the contributions from the sample in the ground and excited states, as well as the cross terms (see Section S2 of the ESI†). Therefore, $C_{\text{diff}}^n(q_1, q_2, t)$ can, in general, have nonzero values at $t < 0$. In practice, the pump-induced time-dependent contribution can be determined from the measured $C_{\text{diff}}^n(q_1, q_2, t)$ as,

$$C_{\text{td}}^n(q_1, q_2, t) = \widetilde{C}_{\text{diff}}^n(q_1, q_2, t) - \widetilde{C}_{\text{diff}}^n(q_1, q_2, t < 0), \tag{4}$$

where the tilde "$\sim$" denotes the statistically averaged quantities. Statistical averaging can be performed at each t over a set of M_t difference images determined in the appropriately chosen range of pump-probe delay times $[t_1, t_2)$, $\widetilde{C}_{\text{diff}}^n(q_1, q_2, t) = 1/M_t \sum_{t_1 \leq t_i < t_2} C_{\text{diff}}^n(q_1, q_2, t_i)$, while formally assuming $t = (t_1 + t_2)/2$. According to its definition in Eq. (4), $C_{\text{td}}^n(q_1, q_2, t)$ can have nonvanishing values only at $t \geq 0$, and thus can be used to analyze the pump-induced contribution to the correlation function $C_{\text{diff}}(q_1, q_2, \Delta, t)$.
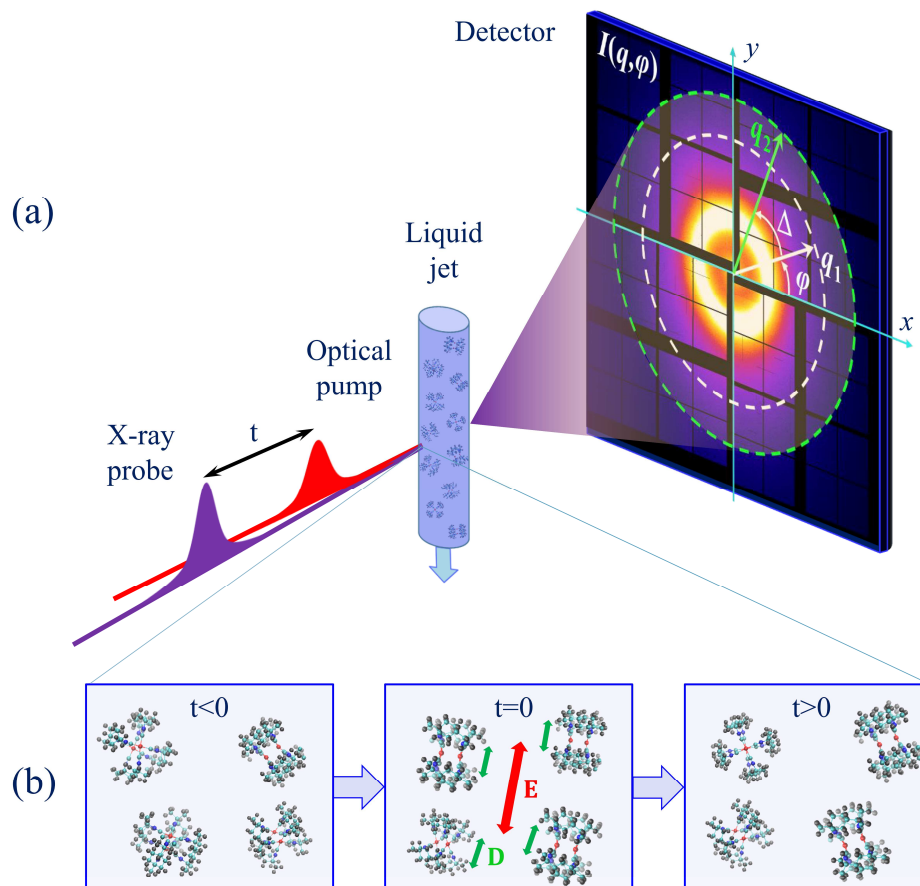
Fig. 2 Scheme of the pump-probe experiment on $[Ir_2(dimen)_4]^{2+}$. (a) Experimental setup. An optical pump triggers the dynamics in the sample solution delivered in a liquid jet, that is subsequently probed by an x-ray pulse following at a time delay t after the optical pulse. Diffuse scattering patterns $I(q,\varphi)$ are recorded on a large area ePix10K detector at different delays t. Vectors $\mathbf{q_1}$ and $\mathbf{q_2}$, as well as the angles φ and Δ indicated on the detector image are used in the definition of the CCF in Eq. (2). (b) A sketch of the sample dynamics. Before the optical excitation ($t < 0$) all molecules are in the ground state (GS) and have random orientations. Optical laser pulse at $t = 0$ selectively promotes $[Ir_2(dimen)_4]^{2+}$ molecules to the metastable excited state (ES), forming $\cos^2 \Psi$ distribution of the excited molecules, where Ψ is the angle between the TDM $\mathbf{D}$ of a molecule and polarization direction $\mathbf{E}$ of the optical pulse. This leads to an anisotropy in the measured x-ray scattered patterns, which decays on the time scale of rotational motions of the excited molecules. At later times ($t > 0$) the molecular system eventually relaxes to the ground state.

5   Experimental results

The experimental difference images $I_{\text{diff}}(q,\varphi,t)$ were sorted in pump-probe delay time bins of equal width $t_2 - t_1 = 100$ fs in the range from -0.5 to 2.5 ps, giving about $M_t = 10^4$ images per time bin t. Difference intensities averaged over 500 images at each t are shown for selected delay times in Fig. 3. For each time bin the statistical averaging of the difference intensities was performed over M_t patterns, $\widetilde{I}_{\text{diff}}(q,t) = 1/M_t \sum_{t_1 \leq t_i < t_2} I_{\text{diff}}(q,t_i)$, with $t = (t_1 + t_2)/2$. Both the averaged difference images in Fig. 3 and azimuthally averaged difference intensity $\widetilde{I}_{\text{diff}}(q,t)$ shown in Fig. 4 for -0.5 ps $< t <$ 2.5 ps reveal a time-dependent signal that starts to evolve immediately after the excitation at $t = 0$, indicating the pump-induced structural changes in the system.

The $q-$ and $t-$dependent difference intensity $\widetilde{I}_{\text{diff}}(q,t)$ is employed in the basic analysis of the photoinduced dynamics[72]. Alternatively, one can apply Legendre polynomial expansion of the difference images $I_{\text{diff}}(q,\varphi,t)$ [see Eq. (1)] to gain additional information by separating the isotropic and anisotropic contributions to the difference intensity[45,47–49]. In this work we ex-

plore the pump-induced changes by determining $\widetilde{C}_{\text{diff}}^n(q_1,q_2,t)$ and $C_{\text{td}}^n(q_1,q_2,t)$ from the experimental data using Eqs. (2)-(4). In the case of computation of $\widetilde{C}_{\text{diff}}^n(q_1,q_2,t<0)$ we used an extended time range (t_1=-0.4 ps, t_2=-0.15 ps) to improve the signal-to-noise ratio. By considering each FC $C_{\text{td}}^n(q_1,q_2,t)$ [or $\widetilde{C}_{\text{diff}}^n(q_1,q_2,t)$] at a given time delay t for an arbitrary harmonic order n as a two-dimensional (2D) function of (q_1,q_2), the correlation data provide an alternative view of the photoinduced structural dynamics.

In Fig. 5 the experimental values of FCs $|\widetilde{C}_{\text{diff}}^n(q_1,q_2,t)|$ and $|C_{\text{td}}^n(q_1,q_2,t)|$ determined at t=2.0 ps, as well as the time-independent contribution $|\widetilde{C}_{\text{diff}}^n(q_1,q_2,t<0)|$ are presented (see also Section S3 of the ESI[†]). A relatively high magnitude of the time-independent contribution $|\widetilde{C}_{\text{diff}}^n(q_1,q_2,t<0)|$ observed in our measurements (see Fig. 5b) might be associated with the equilibrium solvent or solvent-solute interactions, and possibly also includes remaining uncompensated background contributions. This contribution can be removed by applying Eq. (4) to access the time-dependent part $C_{\text{td}}^n(q_1,q_2,t)$ (Fig. 5c). As one can see, the strongest contribution to $C_{\text{td}}^n(q_1,q_2,t)$ is defined by FCs of the or-
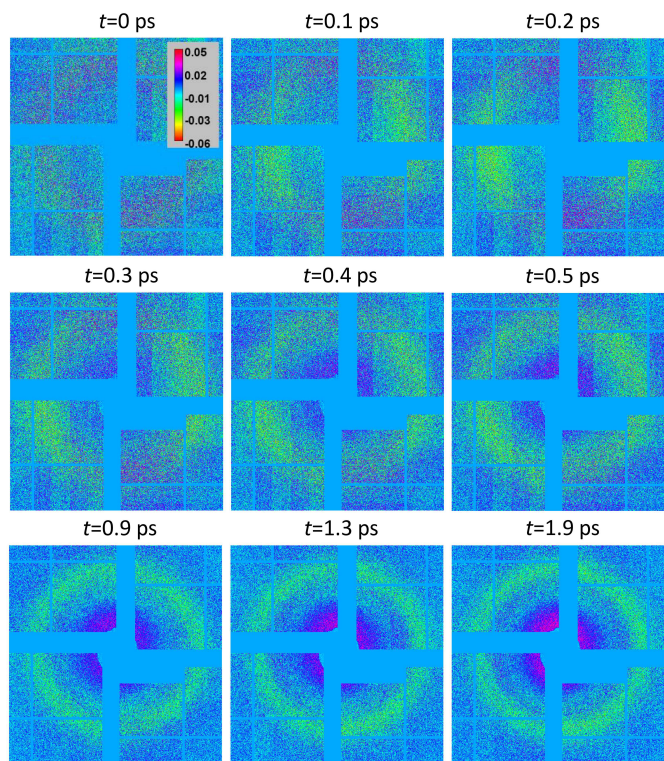
Fig. 3 Averaged difference scattering images $\widetilde{I}_{\mathrm{diff}}(q,\varphi,t)$ from $[\mathrm{Ir}_2(\mathrm{dimen})_4]^{2+}$ in acetonitrile shown for selected pump-probe delay times t. Each image shows the region of interest around the origin of reciprocal space extending up to 2.2 Å^{-1} at the edges of each image, where the most prominent intensity changes can be observed.

Fig. 4 Difference scattering intensity $\widetilde{I}_{\mathrm{diff}}(q,t)$ experimentally determined for $[\mathrm{Ir}_2(\mathrm{dimen})_4]^{2+}$ in acetonitrile in the range of pump-probe delay times t from -0.5 to 2.5 ps.

ders $n=0$ and $n=2$, while other orders are characterized with vanishing magnitudes. This observation is in agreement with the results of Legendre polynomial analysis of TRXSS intensity, where orientations of molecules in the excited state obey the cosine squared distribution[45], thus leading to nonvanishing contributions of the zero-order and 2nd order polynomials.

The evolution of the time-dependent term $C_{\mathrm{td}}^n(q_1,q_2,t)$ determined for our system as a function of the pump-probe delay time t is shown in Fig. 6 for $n=0$, and in Fig. 7 for $n=2$. As one can see, the most prominent changes in time are observed for FC of the order $n=0$, while the correlation maps for $n=2$ contain less pronounced, yet clearly distinguishable features. Overall, the magnitude of $|C_{\mathrm{td}}^0(q_1,q_2,t)|$ rapidly grows after excitation during the first picosecond, and remains at about the same level during the second picosecond (see Fig. 6). One can also see a delayed and slowly rising signal in the low q region of $|C_{\mathrm{td}}^2(q_1,q_2,t)|$ at $t>0.5$ ps (see arrows in Fig. 7), that may be also attributed to the structural dynamics of $[\mathrm{Ir}_2(\mathrm{dimen})_4]^{2+}$ in acetonitrile.

At the same time, a transient increase of $|C_{\mathrm{td}}^2(q_1,q_2,t)|$ can be observed in the region around $q_1=q_2=1.7$ Å^{-1}, reaching
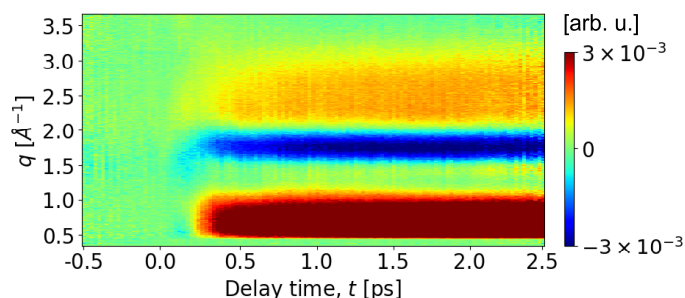
the maximum amplitude at about $t=200$ fs (denoted with a dashed circle in Fig. 7). In addition to the dominant FCs of the orders $n=0$ and $n=2$, we also detected very weak contributions of FCs of the higher orders $n=6$ and $n=10$, which peak at about $t=200$ fs [see Fig. 8]. In order to detect weak higher-order contributions we used the integrated quantities, $S_{\mathrm{td}}^n(t)=\int_{q_1}\int_{q_2}|C_{\mathrm{td}}^n(q_1,q_2,t)|^2dq_1dq_2$, with the integration range 1.1 Å$^{-1}\leq q_1,q_2\leq 2.1$ Å^{-1} defined around the round feature observed in $|C_{\mathrm{td}}^2(q_1,q_2,t)|$ (see a dashed circle in Fig. 7). Similar behavior of $S_{\mathrm{td}}^n(t)$ observed in the sub-ps time range both for the sample solution [Fig. 8(a)] and pure acetonitrile [Fig. 8(b)] allows us to attribute this feature to ultrafast solvent excitation.

Recently, multiple order contributions in the Legendre polynomial decomposition of the difference intensity have been reported in the ultrafast pump-probe experiment on the gas phase molecules and attributed to the multi-photon processes[49]. Sequential appearance of FCs of multiple orders (e.g, $n=6$, 12, 18, 24, starting from the lowest order $n=6$) is a characteristic signature of the increasing orientational order in the material, for instance as it was shown in the studies of the smectic-hexatic phase transitions in liquid crystals[56,57]. In the present case of acetonitrile, the situation is different since, considering $n=2$ is the lowest nonvanishing order, the FCs of the orders $n=4$ and $n=8$ have vanishing values, and at the same time a weak but detectable contribution is observed for the orders $n=6$ and $n=10$. Such selective appearance of higher-order FCs in our experiment points toward a different origin, e.g., solvent molecules rearrangements accompanying the optical Kerr effect[73–76], and requires further investigation.

In the present work we focus on characterizing the photoinduced structural changes in the solute subsystem by performing the model assisted analysis of the results shown in Figs. 6 and 7.

6   Simulations

To interpret the experimentally measured correlation data we compared the obtained results with the simulated correlation
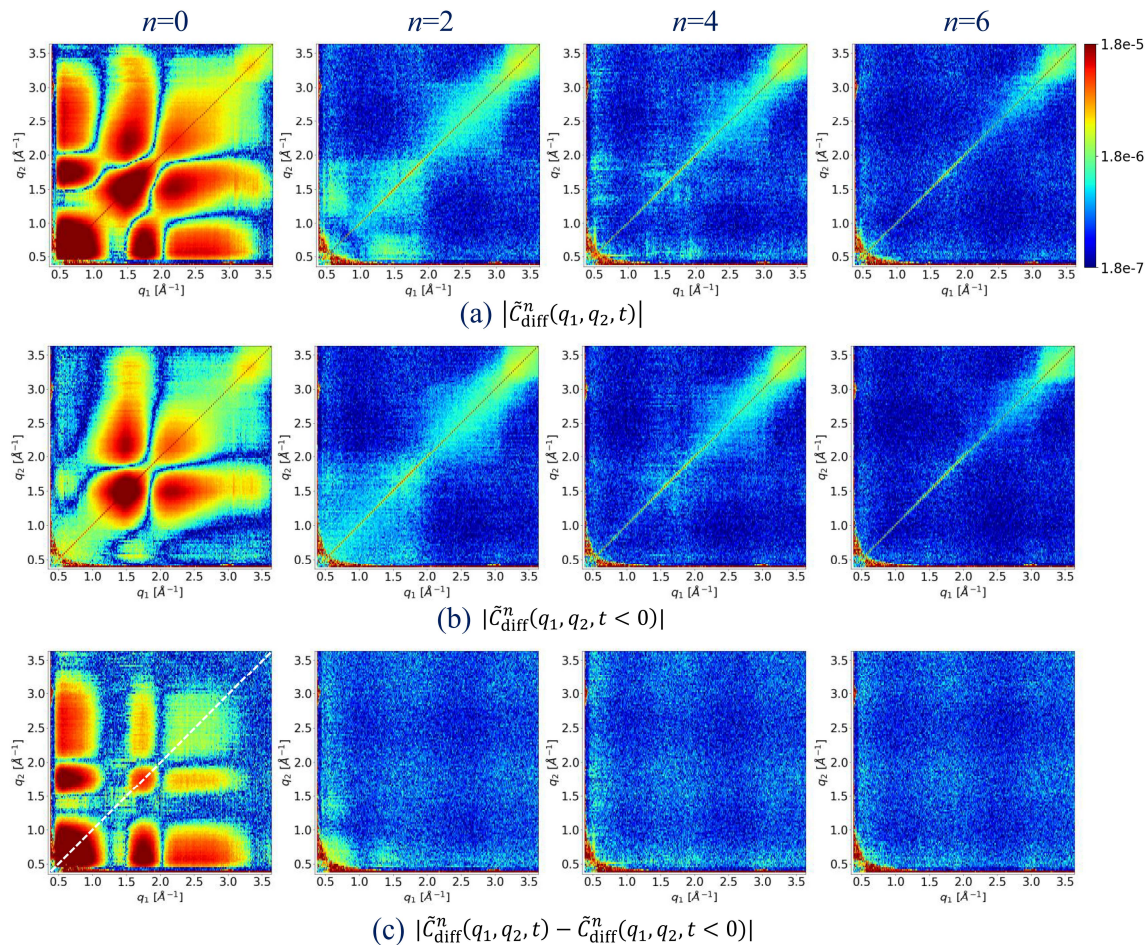
Fig. 5 (Log scale, arb. units) Experimentally determined magnitudes of (a) difference FCs $|\widetilde{C}^n_{\mathrm{diff}}(q_1,q_2,t)|$, as well as (b) time-independent $|\widetilde{C}^n_{\mathrm{diff}}(q_1,q_2,t < 0)|$ and (c) time-dependent FCs $|C^n_{\mathrm{td}}(q_1,q_2,t)| = |\widetilde{C}^n_{\mathrm{diff}}(q_1,q_2,t) - \widetilde{C}^n_{\mathrm{diff}}(q_1,q_2,t < 0)|$ [see Eq. 4], shown in the range $0.3\,\text{Å}^{-1} < q_1,q_2, < 3.6\,\text{Å}^{-1}$ for harmonic orders $n = 0, 2, 4$ and 6. Here, the FCs $\widetilde{C}^n_{\mathrm{diff}}(q_1,q_2,t)$ and $C^n_{\mathrm{td}}(q_1,q_2,t)$ were determined at $t = 2.0$ ps, and $\widetilde{C}^n_{\mathrm{diff}}(q_1,q_2,t < 0)$ was averaged over the time range -0.4 ps $< t <$ -0.15 ps (see the text). The white dashed line in (c) along the direction $q_1 = q_2$ defines the section through the map, which produces the curve at $t = 2.0$ ps shown in Fig. 11(a).

plots for various structural models. This was accomplished by simulating x-ray scattering from different samples, and then computing the correlation functions from the simulated difference scattering images. In our simulations we used atomic models of $[\mathrm{Ir}_2(\mathrm{dimen})_4]^{2+}$ molecules from two different sets of computed structures. The first dataset contains about 120 ground state (GS) and excited state (ES) structures of $[\mathrm{Ir}_2(\mathrm{dimen})_4]^{2+}$ determined in DFT calculations in vacuum as described in Ref.[67]. The second set is based on the 44 trajectories produced in QM/MM BOMD simulations of long $[\mathrm{Ir}_2(\mathrm{dimen})_4]^{2+}$ conformer in acetonitrile reported in Ref.[61]. For convenience, hereafter we will regard these two sets of structures as DFT and BOMD structures. In the case of BOMD simulations, the simulation box contained one $[\mathrm{Ir}_2(\mathrm{dimen})_4]^{2+}$ molecule surrounded by 237 solvent molecules. Each BOMD trajectory represents the sample structure evolution after optical excitation starting from distinct time points of a single 18.2 ps-long equilibrated GS trajectory[61], and contains atomic coordinates of molecules recorded with 1 fs step in the time range from 0 up to about 3.5 ps. Due to the solvent influence, the BOMD structures sample a larger area of the potential energy surface

than the vacuum DFT calculations (see Section S4 of the ESI†).

We performed x-ray scattering simulations of the pump-probe difference intensities $I_{\mathrm{diff}}(\mathbf{q},t)$ from disordered ensembles of $[\mathrm{Ir}_2(\mathrm{dimen})_4]^{2+}$ molecules. The diffraction geometry assumed in our simulations was similar to the one applied in the LCLS experiment: photon energy of 9.5 keV, sample to detector distance of 56 mm, detector with an active area size 165×165 mm (512×512 pixels). The pixel size assumed in simulations is about 3 times larger than in the LCLS experiment to speed up scattering simulations. In our x-ray scattering simulations we considered a fixed number of $N = 10^4$ $[\mathrm{Ir}_2(\mathrm{dimen})_4]^{2+}$ molecules randomly positioned inside a box of a cubic shape of 500 nm in size. We employed composite models, where both $I_{\mathrm{on}}(\mathbf{q},t)$ and $I_{\mathrm{off}}(\mathbf{q})$ were defined in terms of several contributions depending on a particular model (see below for details). We did not include solvent molecules in our diffraction simulations, except of a few model cases considered in Section S6 of the ESI† (see Fig. S7). We used $M = 10^4$ simulated difference scattering patterns $I_{\mathrm{diff}}(\mathbf{q},t) = I_{\mathrm{on}}(\mathbf{q},t) - I_{\mathrm{off}}(\mathbf{q})$ to compute the average $\widetilde{C}^n_{\mathrm{diff}}(q_1,q_2,t)$ for each considered model of the sample.
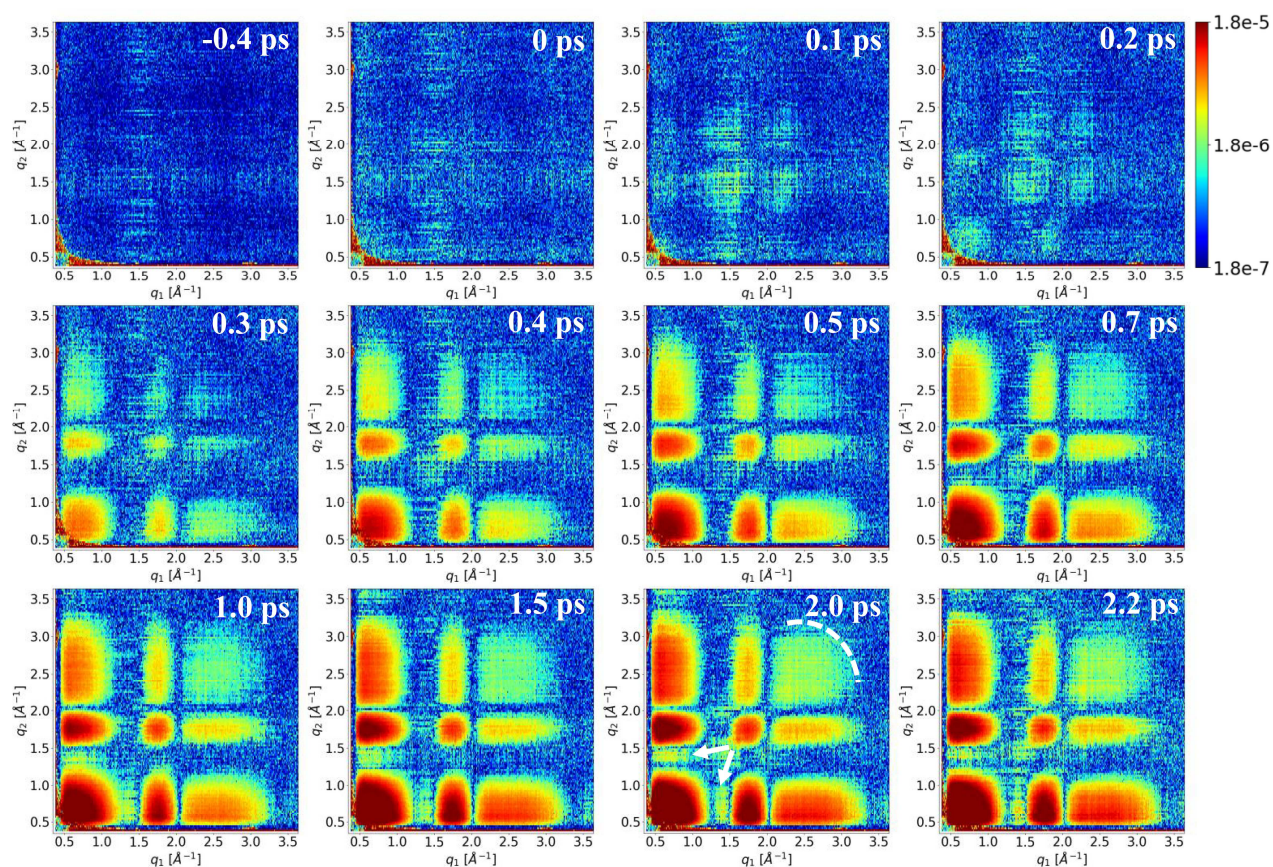
Fig. 6 (Log scale) Evolution of the experimentally determined time-dependent component $|C^0_{td}(q_1, q_2, t)|$ of the order $n = 0$ is shown for several pump-probe delay times in the range $-0.4\,\mathrm{ps} \le t \le 2.2\,\mathrm{ps}$. Features observed in BOMD simulations are indicated with the dashed line and arrows at $t = 2$ ps.

In the following subsections we investigate various aspects of the photoinduced dynamics in the ensembles of $[\mathrm{Ir}_2(\mathrm{dimen})_4]^{2+}$ molecules, including the orientations of the TDMs, excitation fractions of distinct GS populations, as well as atomic disorder in the molecules.

6.1 Transition dipole moments

Identification of the orientation of the optical transition dipole moment (TDM) in the ultrafast time-resolved x-ray measurements can be quite challenging[77]. Here we show that the TDM orientations can be determined from the angular correlation functions. We investigate excitation scenarios involving various distributions of the TDMs, where we employ the set of structures from DFT calculations.

In the simulations of difference intensities $I_{\mathrm{diff}}(\mathbf{q}, t)$ from the DFT structures at a particular time t we operated with two GS ($\mathrm{GS_{SH}}$ and $\mathrm{GS_{LG}}$) and one ES structures. While both GS structures are time-independent, the interatomic Ir-Ir distance and N-Ir-Ir-N dihedral angle in the ES structure depends on the pump-probe delay time t, as it was determined in Ref.[67]. We assumed that in the unpumped sample the two ground states $\mathrm{GS_{SH}}$ and $\mathrm{GS_{LG}}$ are represented in equal proportion[64,78] ($N_{\mathrm{GS_{SH}}} = N_{\mathrm{GS_{LG}}} = N/2 = 5 \times 10^3$), and orientations of the GS molecules are distributed uniformly on the 3D rotation group SO(3). The GS molecules

are selectively excited by a linearly polarized optical pump, with a probability proportional to $\cos^2 \Psi$. The excitation probability $p < 1$, and the number of excited particles is $N_{\mathrm{ES}} = pN$. The remaining fraction $(1 - p)$ of non-excited molecules remain in $\mathrm{GS_{SH}}$ and $\mathrm{GS_{LG}}$ states in equal proportions, i.e. after the excitation $N_{\mathrm{GS_{SH}}} = N_{\mathrm{GS_{LG}}} = (1 - p)N/2$.

We assume the dilute limit approximation, where the average distance between the solute molecules is much larger compared to their sizes, and simulate the "laser-off" and "laser-on" scattered intensities at a particular time delay as (here we omit the q and t dependence in the expressions of intensities for clarity of presentation),

$$I_{\mathrm{off}} = I(\mathrm{GS_{SH}}, \tfrac{N}{2}, \mathrm{Uniform}) + I(\mathrm{GS_{LG}}, \tfrac{N}{2}, \mathrm{Uniform}), \quad (5)$$

$$I_{\mathrm{on}} = I(\mathrm{ES}, pN, \cos^2 \Psi) + I(\mathrm{GS_{SH}}, [1 - p]\tfrac{N}{2}, \mathrm{Uniform})$$

$$+ I(\mathrm{GS_{LG}}, [1 - p]\tfrac{N}{2}, \mathrm{Uniform}), \quad (6)$$

where, for instance, the notation $I(\mathrm{GS_{SH}}, \tfrac{N}{2}, \mathrm{Uniform})$ defines the scattered intensity calculated from $N/2$ identical molecules in the ground state $\mathrm{GS_{SH}}$ with a uniform distribution of molecular orientations, and $I(\mathrm{ES}, pN, \cos^2)$ defines the scattering intensity calculated from pN identical molecules in the excited state ES, with
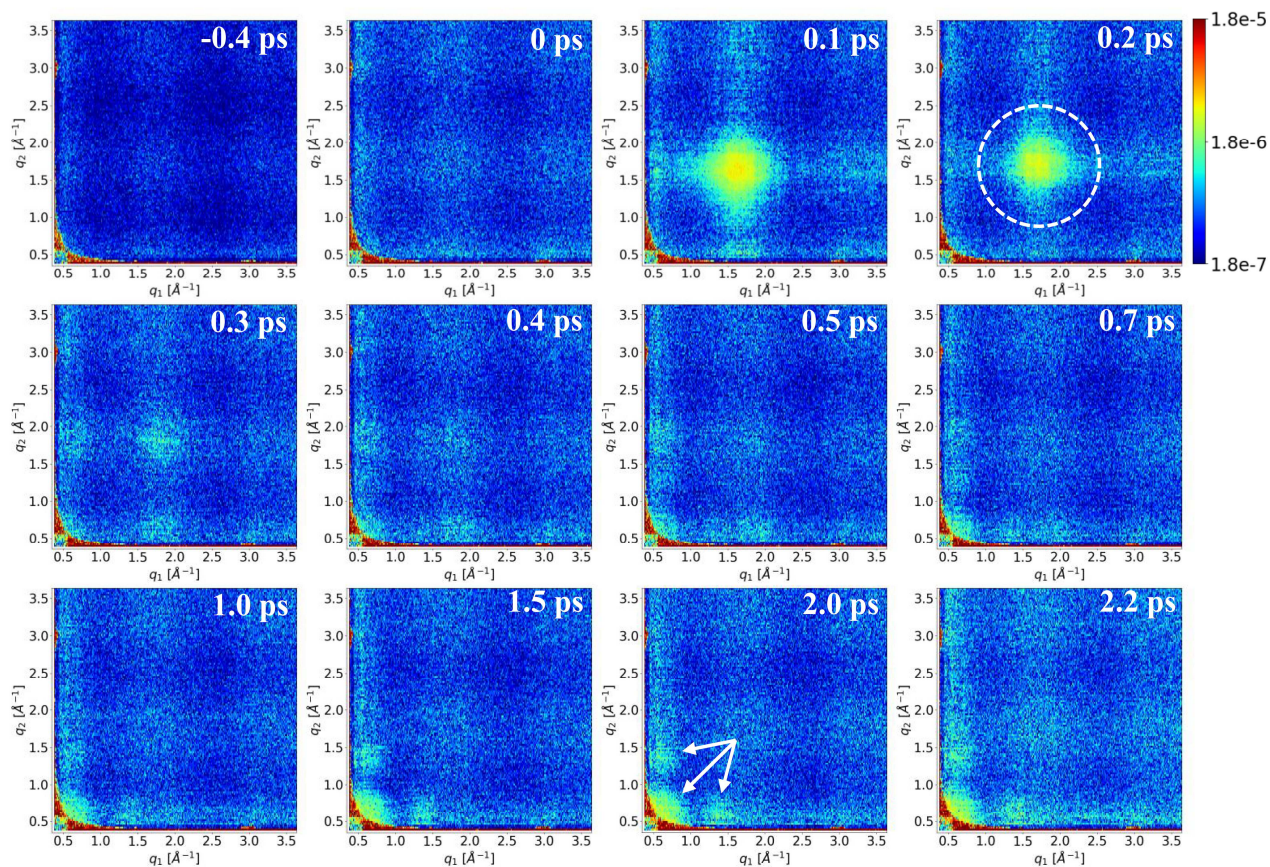
Fig. 7 (Log scale) Evolution of the experimentally determined time-dependent component $|C^2_{\mathrm{td}}(q_1,q_2,t)|$ of the order $n=2$ is shown for several pump-probe delay times in the range $-0.4\,\mathrm{ps} \le t \le 2.2\,\mathrm{ps}$. Features indicated with a dashed circle and arrows are discussed in the text.

$\cos^2\Psi$ distribution of orientations of the molecules.

We examined several distinct cases of the TDM orientations in the excited state, assuming the excitation fraction of 10% ($p = 0.1$) in Eq. (6). We constructed three different models, ES_1, ES_{1a}, ES_{1b}, with the direction of the TDMs perpendicular to the Ir-Ir axis, as well as the ES_2 model with the direction of the TDMs parallel to the Ir-Ir axis. Geometric considerations used to generate orientational distribution of the molecules for these four models are presented in Fig. 9 and described below. In the ES_{1a} model we assumed that the TDMs $\mathbf{D}$ are oriented perpendicular to the Ir-Ir bond, and are aligned with a chosen Ir-C-N ligand bridge, as it is shown in the inset of Fig. 9(a). The orientations of the $N_{\mathrm{ES}} = pN$ excited molecules were generated in such a way that orientations of their TDMs obey $\cos^2\Psi$ distribution, where Ψ is an angle between the TDM $\mathbf{D}$ and polarization axis $\mathbf{E}$ of the optical laser pulse. The model ES_{1b} is a "four-fold degenerate" variant of the model ES_{1a}, where the orientation of the TDM can take with equal probability any of four distinct directions along the Ir-C-N ligand bridges. That is, the angle θ [see the inset in Fig. 9(a)] takes with equal probability one of the four values, $\theta \in \{\theta_0, \theta_0 + \frac{\pi}{2}, \theta_0 + \pi, \theta_0 + \frac{3\pi}{2}\}$, where θ_0 corresponds to the direction pointing towards a chosen (reference) Ir-C-N ligand bridge. In the most "disordered" model ES_1 with the TDM orientation perpendicular to the Ir-Ir axis, we assumed that the angle

θ can take any value in the range $[0, 2\pi)$ with equal probability, thus the distribution of the TDMs is circular isotropic about the Ir-Ir axis. Finally, in the ES_2 model we considered an orthogonal case where the TDMs are oriented parallel to the Ir-Ir bond [see Fig. 9(b)].

The intensity scattered from pN molecules in the excited state $I(\mathrm{ES}, pN, \cos^2)$ [see Eq. (6)] was determined by considering one of the orientational distributions of molecules (ES_1, ES_{1a}, ES_{1b}, or ES_2). All scattering contributions from the GS molecules in Eqs. (5) and (6) were computed by assuming that the molecules have random positions and their orientations are uniformly distributed on SO(3). Using Eqs. (1), (5), and (6) we simulated $M = 10^4$ difference images $I_{\mathrm{diff}}(q, \varphi, t)$ for each model, and then computed averaged FCs $\widetilde{C}^n_{\mathrm{diff}}(q_1, q_2, t)$. The magnitudes of FCs of the orders $n = 0, 2$ and 4 determined at $t = 2$ ps for ES_1, ES_{1a}, ES_{1b}, and ES_2 models are shown in Fig. 10.

As one can see, the plots of $|\widetilde{C}^0_{\mathrm{diff}}(q_1, q_2, t)|$ at $n = 0$ determined for the models ES_1, ES_{1a}, and ES_{1b} [Figs. 10(a-c)] are in good agreement with the experimental result $|C^0_{\mathrm{td}}(q_1, q_2, t)|$, [see Fig. 5(c)], in contrast to the ES_2 model [Fig. 10(d)]. This is also clearly visible from the line sections of the experimental and simulated correlation plots for $n = 0$ along the direction $q_1 = q_2 = q$ shown in Figs. 11(a) and 11(b), respectively. Comparison of the experimental plots of $|C^0_{\mathrm{td}}(q_1, q_2, t)|$ [Fig. 11(a)] and simulated
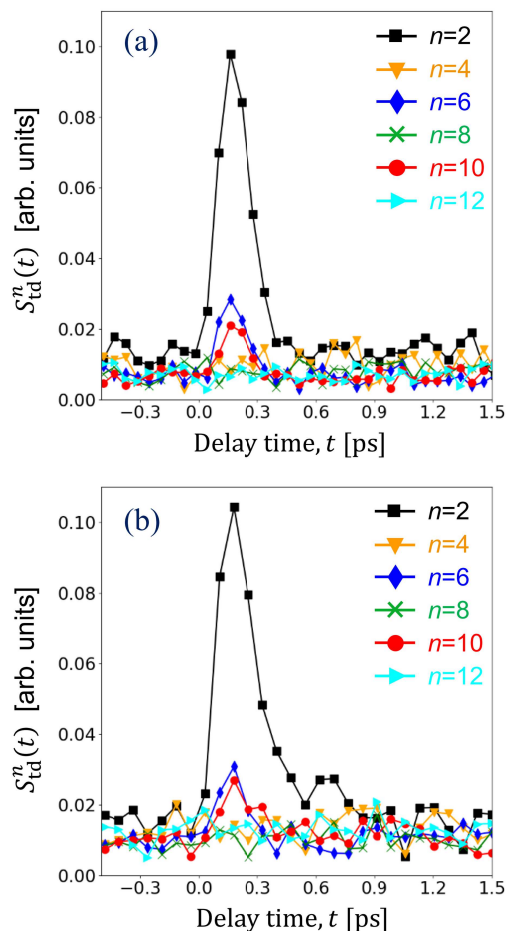
Fig. 8 Experimental values $S_{\text{td}}^n(t)$ for the FC orders $n = 2, 4, 6, 8$ and 10 determined for solution of $[\text{Ir}_2(\text{dimen})_4]^{2+}$ in acetonitrile (a) and for pure acetonitrile (b).

$|\widetilde{C}_{\text{diff}}^0(q_1, q_2, t)|$ [Fig. 11(b)] shows better agreement of the ES_1, ES_{1a}, and ES_{1b} models with the experimental data, as compared to the ES_2 model. Thus, a characteristic fingerprint in the plot of FC of the order $n = 0$ allows us to unambiguously identify that after excitation with a 398 nm optical laser, the TDMs of the molecules are predominantly oriented perpendicular to the Ir-Ir axis. The simulated FCs of the order $n = 2$ agree only partially with the experimental results, showing similar features in the low q region [noted with white arrows in Fig. 7 and Fig. 10(a)]. Finally, a relatively weak magnitude of FC of the order $n = 4$ in the case of the model ES_1 [see Fig. 10(a)], as well as a less pronounced bump at about $q = 1.3$ Å^{-1} [noted by a green arrow in Fig. 11(b)], makes this model more compatible with the experimental result [see Figs. 5(c) and 11(a)], as compared to the ES_{1a} and ES_{1b} models. The latter observation points toward the isotropic distribution of TDMs about the Ir-Ir axis, rather than aligned TDMs in a specific direction.

In addition to the models ES_1 and ES_2, we also tested a model with coexisting orthogonal orientations of the TDMs, with distinct probabilities p_1 and p_2 of the ES_1- and ES_2-type excitations, respectively (see Section S5 and Fig. S5 in the ESI†). The results are consistent with the UV-Vis spectroscopy measurements[66], i.e.,

by exciting $[\text{Ir}_2(\text{dimen})_4]^{2+}$ with 398 nm optical laser one predominantly creates the TDMs oriented perpendicular to the Ir-Ir bond, as it is considered in the ES_1 model. In the UV-Vis absorption spectrum of $[\text{Ir}_2(\text{dimen})_4]^{2+}$ the wavelength of 398 nm is located on the shoulder of the UV band centered at 375 nm (see Section 2), where the expected excitation pathway is predominantly of $^3\text{d}\pi \to \text{p}\sigma$ character, with TDMs oriented perpendicular to the Ir-Ir axis.

6.2 Excitation probabilities

Here we consider how variation of the excitation probabilities of two distinct $[\text{Ir}_2(\text{dimen})_4]^{2+}$ conformers is reflected in the results of the cross-correlation analysis. For this purpose we employed the set of structures from DFT calculations considered above. Results of simulations for the ES_1 model at several distinct excitation fractions ($p = 5\%, 10\%, 15\%$, and $p = 20\%$) assumed in Eq. (6) show that the magnitude of $|\widetilde{C}_{\text{diff}}^n(q_1, q_2, t)|$ grows with the increasing excitation fraction p, as it is expected for a system with increasing degree of orientational order (see Section S5 and Fig. S6 in the ESI†).

So far, we assumed in Eq. (6) that the molecules in the ground states GS_{SH} and GS_{LG} are excited with equal probability. Here we consider distinct probabilities, p_{SH} and p_{LG}, for excitations of the "short" GS_{SH} and "long" GS_{LG} conformers, respectively. Within such a model the "laser-on" intensity was determined as

$$I_{\text{on}} = I(\text{ES}, pN, \cos^2 \Psi) + I(\text{GS}_{\text{SH}}, [1 - p_{\text{SH}}]\frac{N}{2}, \text{Uniform})$$

$$+ I(\text{GS}_{\text{LG}}, [1 - p_{\text{LG}}]\frac{N}{2}, \text{Uniform}), \tag{7}$$

with the total excitation fraction $p = p_{\text{SH}} + p_{\text{LG}}$. The calculated correlations maps for distinct values of p_{SH} and p_{LG} are presented in Fig. 12.

The results shown in Fig. 12 look, at first glance, very similar for different models, while the distribution of intensity on the plots of $|\widetilde{C}_{\text{diff}}^0(q_1, q_2, t)|$ for two opposite cases ($p_{\text{LG}} > p_{\text{SH}}$ and $p_{\text{LG}} < p_{\text{SH}}$) [see the regions highlighted with dotted curves in Figs. 12(b) and 12(c)] reveal better agreement of the model where $p_{\text{LG}} = 10\%$ and $p_{\text{SH}} = 1\%$ with the experimental data [compare with the plot of $|C_{\text{td}}^0(q_1, q_2, t)|$ in Fig. 5(c)]. This also follows from the comparison of the line sections at $q_1 = q_2$ of the experimental $|C_{\text{td}}^0(q_1, q_2, t)|$ [Fig. 11(a)] and simulated FCs $|\widetilde{C}_{\text{diff}}^0(q_1, q_2, t)|$ [Fig. 11(c)], where the model with predominant excitation of the "long" conformer clearly shows several features also observed in the experimental data. Considering three pronounced oscillations along q on each curve in Fig. 11(a), one may notice that both, the experimental curves and simulated profile at $p_{\text{LG}} > p_{\text{SH}}$ [red curve with star-shaped markers in Fig. 11(c)], have a more parabolic-like profile of the first oscillation at low q, a small kink on the left site of the middle oscillation at about $q = 1.5$ Å^{-1}, as well as a positive skew in the last oscillation (schematically denoted in Fig. 11(a) with two dashed green curves and an arrow). Thus, the simulated $|\widetilde{C}_{\text{diff}}^0(q_1, q_2, t)|$ are quite sensitive to the variation of the excitation fractions of different conformers, suggesting that the "long" conformer is preferentially excited in
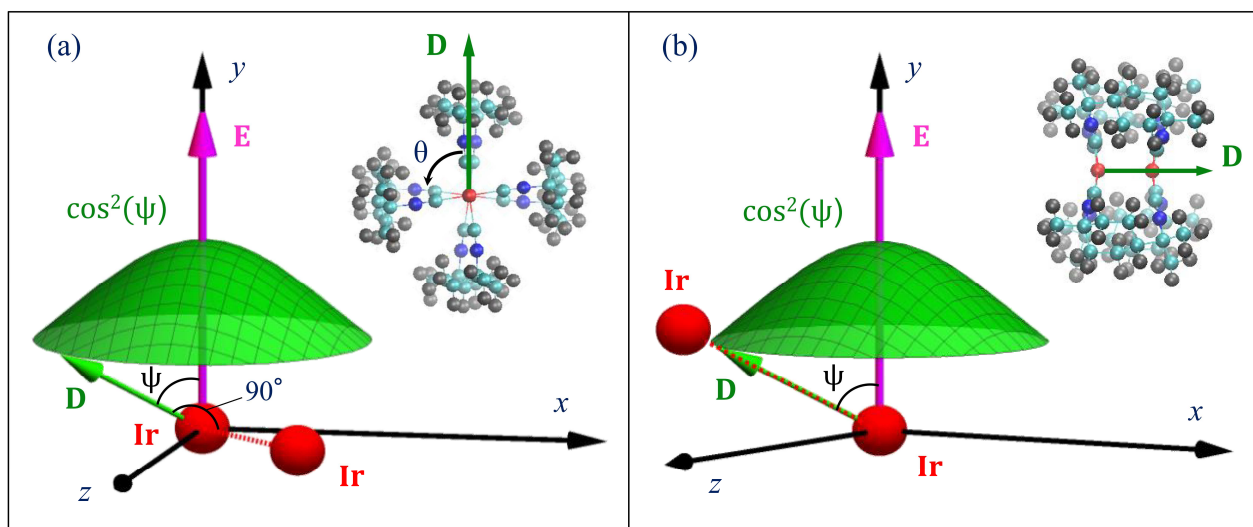
Fig. 9 Orientational distribution of the excited molecules in the sample models ES_1, ES_{1a}, ES_{1b} (a) and ES_2 (b). Two orthogonal cases of the TDM direction **D**, perpendicular (a) and parallel (b) to the Ir-Ir axis of $[Ir_2(dimen)_4]^{2+}$, are illustrated. The **x**, **y** and **z** axes represent a fixed laboratory frame, where the incident x-ray beam propagates in the **z** direction. The optical laser pulse with the polarization axis **E** parallel to the **y** direction creates excited state population with $\cos^2 \Psi$ distribution of orientations of the TDMs, where Ψ is an angle between **D** and **E**.

our experiment.

Recall that two GS conformers can be selectively excited in the visible range 450-650 nm (see Section 2). For instance, in the previous pump-probe XFEL experiment on $[Ir_2(dimen)_4]^{2+}$ with the optical pump ($\lambda = 480$ nm) triggering the $d\sigma^* \to p\sigma$ transitions, the estimated excitation fraction of $[Ir_2(dimen)_4]^{2+}$ molecules was notably larger for the "long" conformer, as compared to the "short" conformer[67]. However such selectivity is seemingly absent in the UV range (300–400 nm), where both conformers absorb at virtually identical wavelengths[66]. At the same time, the time-dependent density functional theory (TDDFT) calculations of the oscillator strengths indicated preferential absorption in the UV range by the "long" conformer[66]. The results of our pump-probe experiment ($\lambda = 398$ nm) are in agreement with these calculations, suggesting that the "long" conformer can be preferentially excited irrespective of the orientation of the TDMs induced by the optical pump.

6.3 Structural disorder

We finally study how heterogeneity and disorder in the structure of the solute molecules manifest themselves in the cross-correlation analysis. For this purpose, we primarily use the structures obtained in QM/MM BOMD simulations of "long" $[Ir_2(dimen)_4]^{2+}$ conformers (GS_{LG}) in acetonitrile[61], and employ a similar modeling approach as described above in Section 6.1. The major difference here is that both GS and ES populations are represented by a larger number of distinct structures extracted from 44 BOMD trajectories, in contrast to two GS structures and a single ES structure (at each t) available from DFT calculations.

We performed x-ray scattering simulations from $[Ir_2(dimen)_4]^{2+}$ molecules only, while acetonitrile molecules surrounding the metal complex in the BOMD simulation box were removed. Notice, while in such simulations the solvent is not contributing directly to the scattered intensity, the effect of solvent on the $[Ir_2(dimen)_4]^{2+}$ molecules, expressed in the bond lengths and angles fluctuations, can still be indirectly captured by x-ray scattering (see a brief discussion of the results with acetonitrile molecules included in the diffraction simulations in Section S6 of the ESI†). The "laser-off" and "laser-on" intensities were computed as follows,

$$I_{off} = I(GS_{LG}, N, Uniform),$$

$$I_{on} = I(ES, pN, \cos^2 \Psi) + I(GS_{LG}, [1-p]N, Uniform), \quad (8)$$
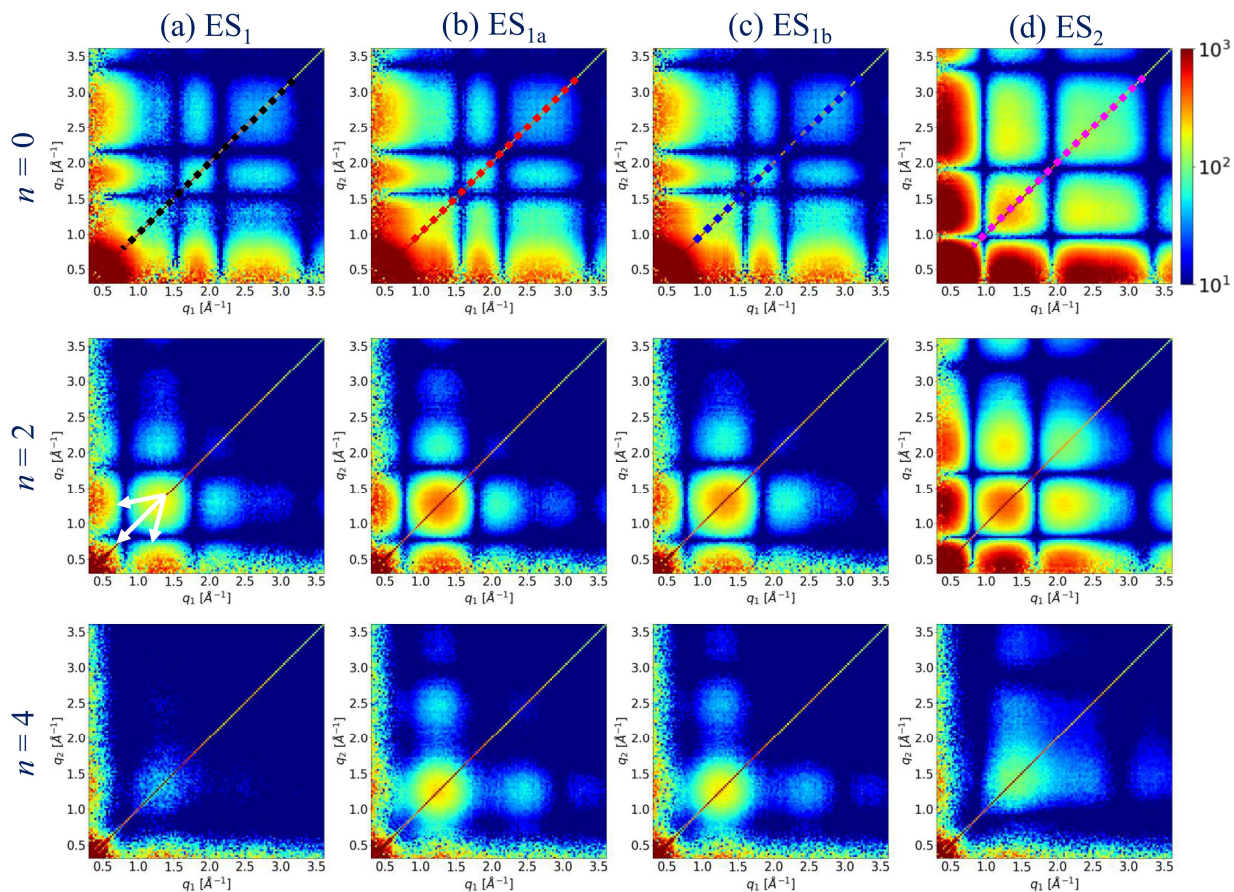
Fig. 10 (Log scale, arb. units) Simulated amplitudes of FCs $|\widetilde{C}_{\mathrm{diff}}^{n}(q_1,q_2,t)|$ of the orders $n=0$, 2 and 4 determined at $t=2$ ps in the range $0.3\,\text{Å}^{-1} \leq q_1, q_2 \leq 3.6\,\text{Å}^{-1}$ for the ES$_1$, ES$_{1a}$, ES$_{1b}$, and ES$_2$ models. The dotted lines in (a)-(c) parallel to the direction $q_1 = q_2$ define the sections through the maps for $n=0$, which produce four curves of the corresponding colors in Fig. 11(b), and the arrows on the map for $n=2$ in (a) denote features discussed in the text.

where the ES$_1$ model with the TDMs oriented perpendicular to the Ir-Ir axis was applied, with a fixed excitation fraction $p=11\%$.

The effect of structural heterogeneity is illustrated on the plots of $|\widetilde{C}_{\mathrm{diff}}^{0}(q_1,q_2,t)|$ shown in Fig. 13 for several representative combinations of the GS and ES structures from the BOMD dataset. A substantial spread of the interatomic distances in the ensemble of BOMD structures (see Section S4 and Fig. S4 in the ESI†) due to thermal solvent influence leads to a significant variation of $|\widetilde{C}_{\mathrm{diff}}^{0}(q_1,q_2,t)|$ determined for distinct selected structures. The results may look notably different even in the cases when the same GS is used [in Eqs. (8)] in combination with distinct ES structures with slightly different distances $d_{\text{Ir-Ir}}$ between the two Ir atoms (compare the plots in individual rows in Fig. 13). Clearly, in such cases a disorder in the ligand structure is fully responsible for the observed differences in the correlation plots.

For certain combinations of the GS and ES structures in Fig. 13 specific fingerprints can be detected, which look similar to the ones observed in the experimental data. For instance, a relatively narrow feature at $q=1.4\,\text{Å}^{-1}$ [denoted with white arrows in Fig. 13 and Fig. 6]. Another peculiarity observed both in the experimental correlation plots and computed for BOMD structures is a rounded corner of the square-shaped region of the zero-order

FCs at large q [denoted with a dashed line in Fig. 13 and Fig. 6]. This highlights the importance of solvent effects in BOMD simulations, where [Ir$_2$(dimen)$_4$]$^{2+}$ structures sample a larger area of the potential energy surface (as compared to vacuum DFT calculations), that enables observation of various features in the correlation plots.

We explored different degrees of freedom in the original BOMD and DFT structures to understand better how variation of distinct structural parameters is reflected in the correlation data. For this purpose we performed x-ray scattering simulations using sets $\{\text{GS}_{\text{LG}}\}$ and $\{\text{ES}\}$ of distinct BOMD structures [in contrast to individual GS$_{\text{LG}}$ and ES structures used in Eqs. (8)], where the "laser-off" and "laser-on" intensities were computed as,

$$I_{\text{off}} = I(\{\text{GS}_{\text{LG}}\}, N, \text{Uniform}),$$

$$I_{\text{on}} = I(\{\text{ES}\}, pN, \cos^2 \Psi) + I(\{\text{GS}_{\text{LG}}\}, [1-p]N, \text{Uniform}) \quad (9)$$

assuming the excitation fraction $p=11\%$. Results of calculations of $|\widetilde{C}_{\mathrm{diff}}^{n}(q_1,q_2,t)|$ for different model cases are presented in Fig. 14, and the corresponding sections through the maps $|\widetilde{C}_{\mathrm{diff}}^{0}(q_1,q_2,t)|$ for $n=0$ along the direction $q_1 = q_2$ are shown in Fig. 11(d).
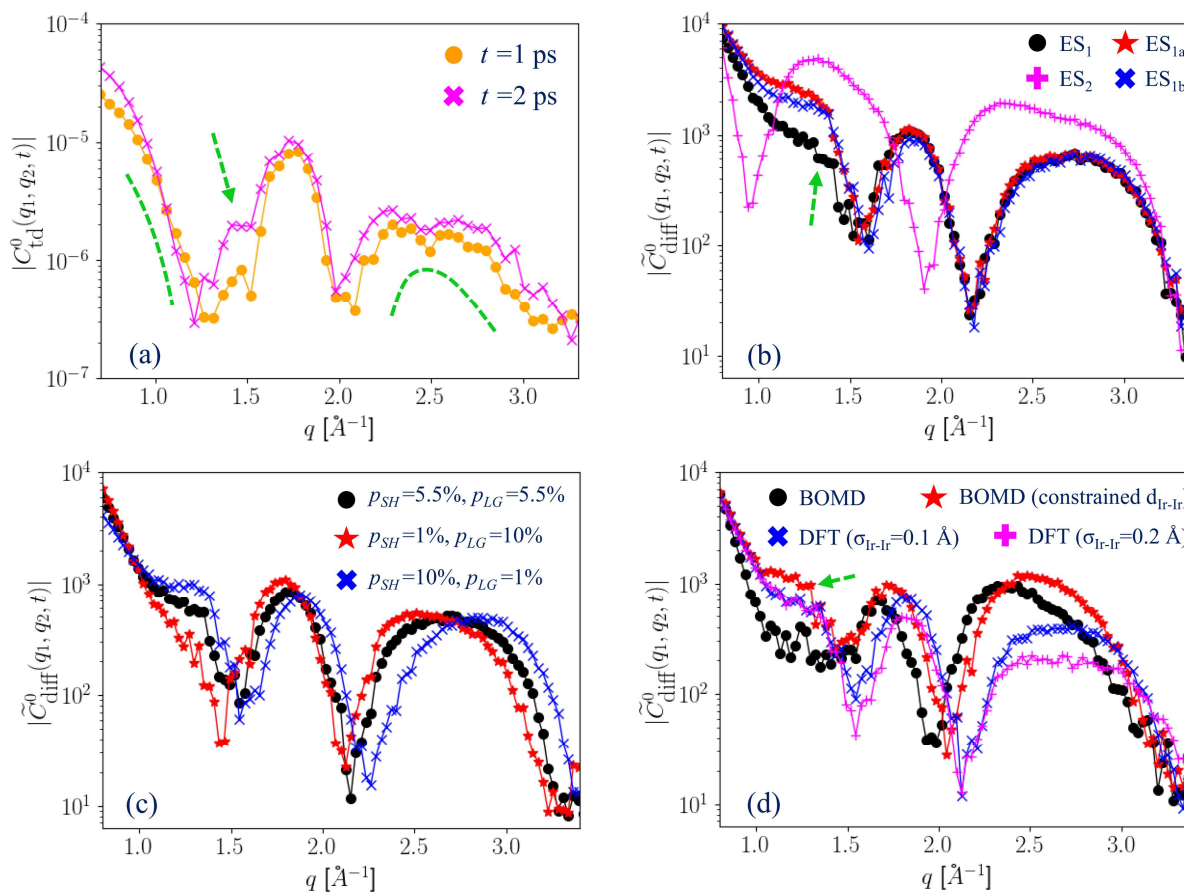
Fig. 11 (Log scale, arb. units) (a) Experimental amplitudes of FCs $|C_{td}^n(q_1, q_2, t)|$ of the order $n = 0$ at $q_1 = q_2 = q$, determined at $t = 1$ ps and $t = 2$ ps. The curves in (a) correspond to the sections of the experimental correlation maps along the direction $q_1 = q_2$ at the respective time delays t [see, e.g. a dashed line in Fig. 5(c) at $t = 2$ ps]. (b-d) Simulated amplitudes of FCs $|\tilde{C}_{diff}^n(q_1, q_2, t)|$ of the order $n = 0$ at $q_1 = q_2 = q$, determined for (b) ES$_1$, ES$_{1a}$, ES$_{1b}$ and ES$_2$ models, (c) three ES$_1$ models with distinct excitation fractions of short (p_{SH}) and long (p_{LG}) conformers, and (d) four models with distinct types of structural disorder in the [Ir$_2$(dimen)$_4$]$^{2+}$ molecules. The plots in (b), (c) and (d) correspond to the sections of $|\tilde{C}_{diff}^0(q_1, q_2, t)|$ along the direction $q_1 = q_2$ shown in Figs. 10(a)-(d), Figs. 12(a)-(c), and Figs. 14(a)-(d), respectively. Green dashed curves and arrows in (a),(b) and (d) denote features discussed in the text.

In Fig. 14(a) the results are shown for a set {GS} with 44 structures and {ES} with 1100 structures extracted from the time interval 2.0 ps $< t <$ 2.03 ps of the BOMD trajectories. Distinct structures from the set {GS} were reused in the same sample multiple times (in random positions and orientations) with approximately equal probability to achieve the required total number $N = 10^4$ of molecules in the sample. The correlation plots in Fig. 14(a) are in reasonable agreement with the results of simulations for DFT structures [see e.g., Fig. 10(a)], as well as experimental results [see Fig. 5(c)], in spite that only the "long" conformer was considered in BOMD simulations. This is another indication that the "long" conformer plays major role in the formation of the excited population of molecules (see Section 6.2).

Next, we performed simulations with the same sets of {GS$_{LG}$} and {ES} atomic structures as in the previous model case [Fig. 14(a)], but manually fixed the Ir-Ir distance to be $d_{Ir\text{-}Ir} = 4.2$ Å in all GS$_{LG}$ structures, and $d_{Ir\text{-}Ir} = 2.9$ Å in all ES structures (here the values of $d_{Ir\text{-}Ir}$ were chosen to be the same as in the GS$_{LG}$ and ES structures from the DFT dataset at $t = 2$ ps). We did not perform structure relaxation after constraining $d_{Ir\text{-}Ir}$ (there-

fore some structures may become chemically unstable), our intent here was to test the sensitivity of correlation approach to the atomic disorder in the ligand structure and variation of the Ir-Ir distance.

The results in Fig. 14(b) show that imposing a constraint on the Ir-Ir distance leads to notable changes in the correlation plots [compare with Fig. 14(a)]. By fixing the Ir-Ir distances we impose structural order on the Ir-Ir bond, which produces the strongest contribution to the scattered intensity. Line sections through the simulated correlation plots shown in Fig. 11(d) reveal that the result for the original BOMD model [circle-shaped markers in Fig. 11(d)] is in better agreement with the experimental results [Fig. 11(a)], compared to the BOMD model with the fixed Ir-Ir bond [star-shaped markers in Fig. 11(d)]. In the latter case, the correlation curve shows less pronounced skew of the last intensity oscillation at high q, as well as a bump at about $q = 1.3$ Å^{-1} [noted by a green arrow in Fig. 11(d)], making this model less consistent with the experimental observations. These results suggest that the experimentally studied solution can be characterized with a notable disorder in the ligand structure and variation of the
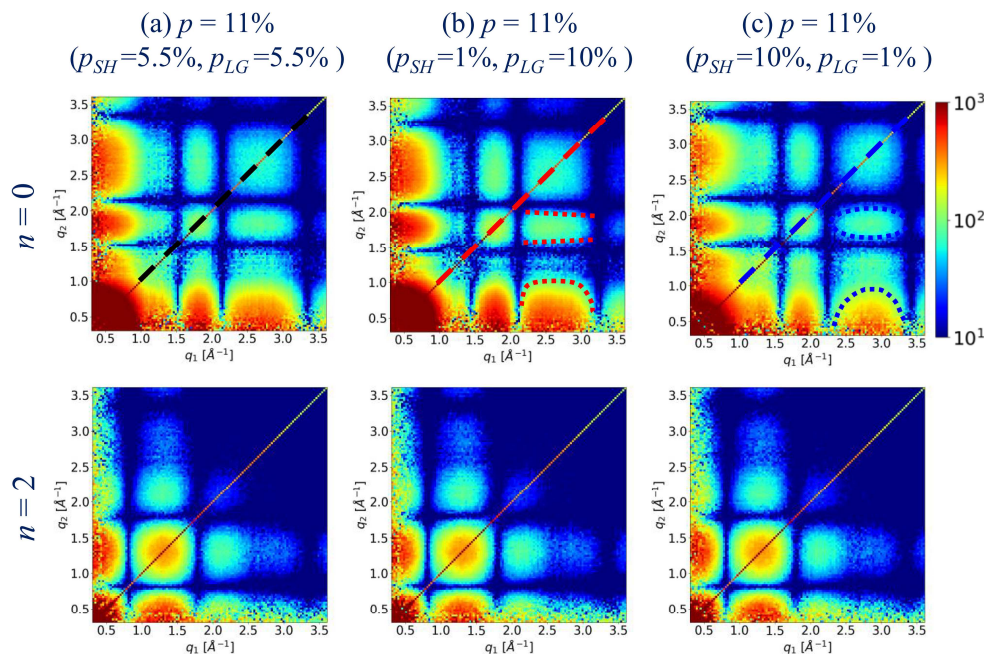
Fig. 12 (Log scale, arb. units) Simulated amplitudes of FCs $|\widetilde{C}^n_{\text{diff}}(q_1,q_2,t)|$ of the orders $n=0$ and $n=2$ determined at $t=2$ ps for different excitation fractions of two ground state populations, p_{SH} and p_{LG}, with $p=p_{SH}+p_{LG}=11\%$. The dashed lines in (a)-(c) parallel to the direction $q_1=q_2$ define the sections through the maps, which produce plots in Fig. 11(c). The dotted curves in (b) and (c) highlight the differences in the distribution of the magnitude of $|\widetilde{C}^0_{\text{diff}}(q_1,q_2,t)|$.

Ir-Ir bond length in $[\text{Ir}_2(\text{dimen})_4]^{2+}$ molecules.

We further explored how variation of the Ir-Ir distance influences the correlations by employing additional sets of structures $\{\text{GS}_{\text{SH}}\}$, $\{\text{GS}_{\text{LG}}\}$ and $\{\text{ES}\}$, using as a basis the two ground state structures, GS_{SH} and GS_{LG}, and one ES structure determined at $t=2$ ps from the DFT dataset presented above (see Section 6.1). The sets of structures $\{\text{GS}_{\text{SH}}\}$, $\{\text{GS}_{\text{LG}}\}$ and $\{\text{ES}\}$ were generated from the respective original DFT structures by replacing the Ir-Ir distance in each $[\text{Ir}_2(\text{dimen})_4]^{2+}$ molecule with $d_{\text{Ir-Ir}}$ sampled from a Gaussian distribution, with a defined mean $\mu_{\text{Ir-Ir}}$ and standard deviation $\sigma_{\text{Ir-Ir}}$. The mean value $\mu_{\text{Ir-Ir}}$ for each of the three datasets was determined by the original Ir-Ir distance of the respective basis DFT structures ($\mu_{\text{Ir-Ir}} = 3.6$ Å for GS_{SH}, $\mu_{\text{Ir-Ir}} = 4.2$ Å for GS_{LG}, and $\mu_{\text{Ir-Ir}} = 2.9$ Å for ES). We performed simulations for different values of the standard deviation $\sigma_{\text{Ir-Ir}}$, in order to impose different degree of structural disorder on the system. The results for $\sigma_{\text{Ir-Ir}} = 0.1$ Å and $\sigma_{\text{Ir-Ir}} = 0.2$ Å are shown in Figs. 14(c) and 14(d), correspondingly. Since the ligand structure is the same for all molecules [within each individual set of structures $\{\text{GS}_{\text{SH}}\}$, $\{\text{GS}_{\text{LG}}\}$ and $\{\text{ES}\}$] in the considered model, the observed changes in the correlation plots can be attributed purely to a different degree of variation of the Ir-Ir bond. As one can see, such type of disorder leads to a faster decrease of the magnitude of $|\widetilde{C}^0_{\text{diff}}(q_1,q_2,t)|$ as a function of q for larger $\sigma_{\text{Ir-Ir}}$ [compare Figs. 14(c) and 13(d)], which is also apparent from the line sections of the respective 2D correlation plots [see Fig. 11(d)].

Visual inspection of all four curves in Fig. 11(d) reveals that the models with a comparably higher degree of structural disorder (in ligands or Ir-Ir bond) are generally characterized with a quicker fall-off of $|\widetilde{C}^0_{\text{diff}}(q_1,q_2,t)|$ as a function of q, as well as broadening and increased skewness of the high-q oscillation. At the same time, models with comparably higher degree of structural order produce an intensity bump in the low-q region at about $q=1.3$ Å^{-1} [noted by a green arrow in Fig. 11(d)], which, however, was not observed in our experiment. Thus, comparison of the characteristic fingerprints in the simulated and experimental correlation data allows us to conclude that the measured ensemble of $[\text{Ir}_2(\text{dimen})_4]^{2+}$ molecules can be characterized with notable variation of the Ir-Ir bond length and disorder in the ligand structures. Such structural disorder can be associated with the solute-solvent interactions[61].

7 Conclusions

In this work we outlined a route for analysis of optically triggered ultrafast dynamics of molecular ensembles in solution, based on the measurements of angular correlations in the scattered x-rays. We applied the correlation approach to characterize structural dynamics of model photocatalyst $[\text{Ir}_2(\text{dimen})_4]^{2+}$ in a pump-probe solution experiment at the LCLS. We performed Fourier analysis of the difference image cross-correlation functions $C_{\text{diff}}(q_1,q_2,\Delta,t)$ and extracted the time dependent contribution $C^n_{\text{td}}(q_1,q_2,t)$, which provides a complex spatiotemporal fingerprint of photoinduced structural dynamics in the system (see Figs. 5-7).

We applied model-assisted analysis of the measured correlation data, by performing simulations of various excitation scenarios with model $[\text{Ir}_2(\text{dimen})_4]^{2+}$ structures determined in DFT and QM/MM BOMD simulations (see Figs. 10-14). The simu-
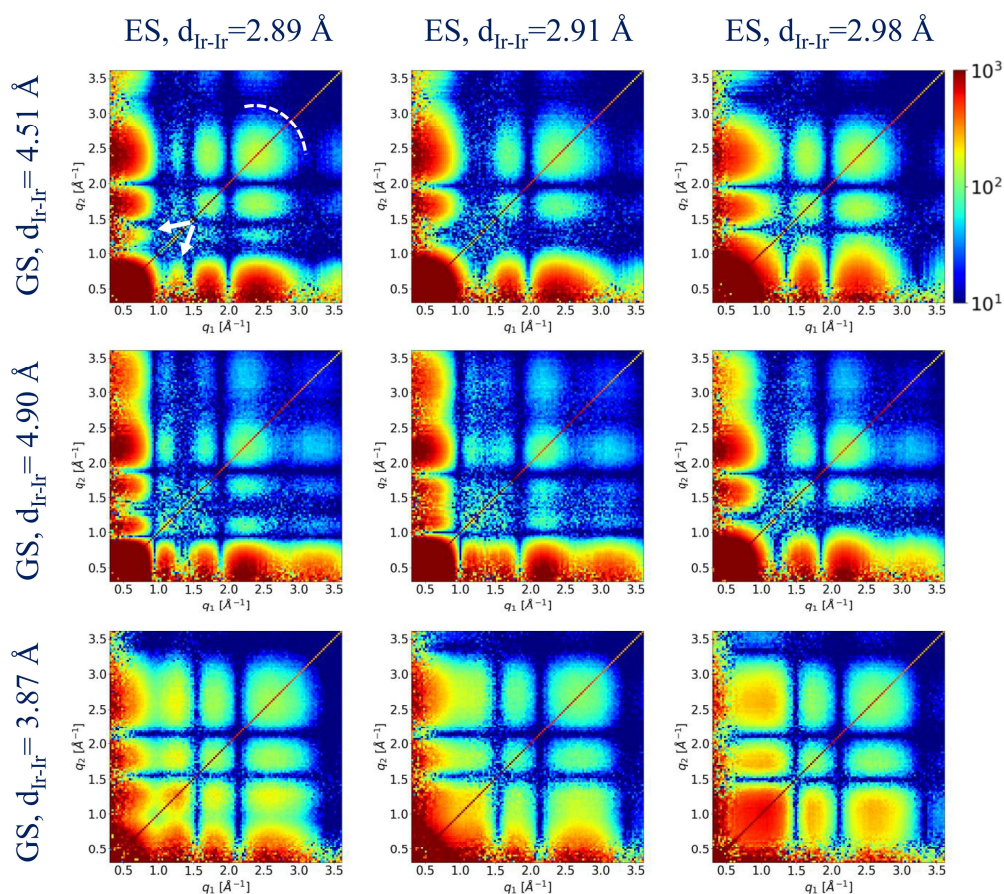
Fig. 13 (Log scale, arb. units) Simulated amplitudes of FCs $|\widetilde{C}^0_{\mathrm{diff}}(q_1,q_2,t)|$ of the order $n = 0$ determined for different combinations of the ES and GS structures from BOMD simulations. The rows correspond to different GS structures, while the columns correspond to different ES structures selected within a 30-fs time bin in the time delay range 2.0 ps $< t <$ 2.03 ps. The distance $d_{\mathrm{Ir\text{-}Ir}}$ between two Ir atoms is specified for each GS and ES structure. The white arrows and dashed curve in (a) highlight features discussed in the text.

lated Fourier spectra $\widetilde{C}^n_{\mathrm{diff}}(q_1,q_2,t)$ appear to be sensitive to various aspects of the ultrafast electron and atomic structure dynamics, including the orientations of the photoinduced TDMs, excitation probabilities of distinct ground state populations, as well as atomic disorder in the solute molecules.

We unambiguously identified that in our experiment the TDMs are preferentially oriented perpendicular to the Ir-Ir axis, and also found that the model with an isotropic distribution of the TDMs around the Ir-Ir bond is in better agreement with the experimental data, as compared to the models with a more defined orientation of the TDMs (see Fig. 10). We also revealed that in our experiment the "long" $[\mathrm{Ir}_2(\mathrm{dimen})_4]^{2+}$ conformer plays major role in the formation of the excited population of molecules, in agreement with TDDFT calculations[66]. A substantial amount of information encoded in the x-ray correlations also allows us to conclude that $[\mathrm{Ir}_2(\mathrm{dimen})_4]^{2+}$ molecules in acetonitrile can be characterized by a substantial structural heterogeneity. Characteristic fingerprints in the simulated and experimental correlation maps suggest a notable variation of the Ir-Ir bond length and disorder in the ligand structures, which can be associated with solvent influence.

It is advantageous to be able to identify various properties of the excited molecular system in a single x-ray experiment with-

out referring to additional measurements/techniques, that may complicate comparison and finding correlations between different observables. For instance, the TDMs are traditionally determined via spectroscopic measurements utilizing polarized light[79], while the correlation approach presented here allows to identify the TDMs along with the ultrafast changes in the atomic structure of the molecules in a single experiment. As we also demonstrated, angular correlation functions can provide complementary information on the excitation probabilities of different molecular conformers, when such information is not easily accessible from the absorption spectroscopy measurements. We find the sensitivity of the correlations to the structural heterogeneity at the atomic scale [see Figs. 13 and 14] quite remarkable, which was not sufficiently explored in the more traditional TRXSS analysis. We showed that the model-assisted analysis of the correlation functions may help to characterize the structural disorder/heterogeneity of the ensemble of molecules, instead of trying to fit the best average structure. The results discussed in relation to the two-dimensional correlation plots shown in Figs. 12 and 13 indicate that the information content in the CCFs may be higher than in the one-dimensional $\Delta S(q)$ curves usually analyzed in TRXSS, and we speculate that this may lead to higher fidelity in the correlation analysis and sensitivity towards, e.g., time evolution of the wave
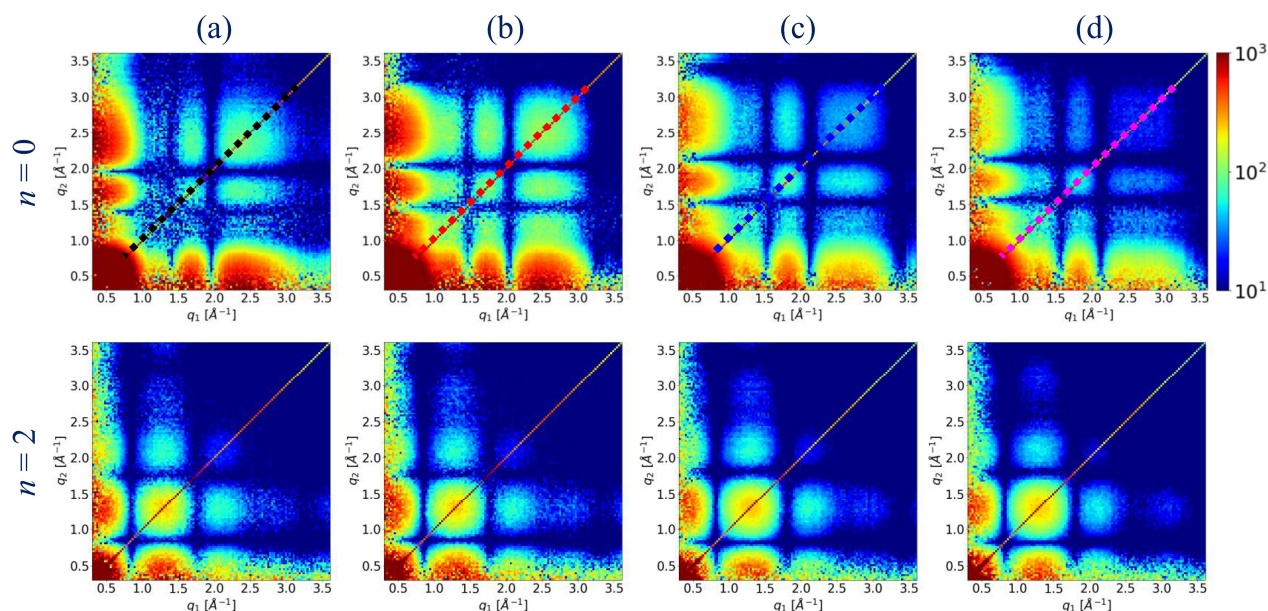
Fig. 14 (Log scale, arb. units) Simulated amplitudes of FCs $|\widetilde{C}_{\text{diff}}^{n}(q_1,q_2,t)|$ of the orders $n=0$ and 2 for different sets of the ground state {GS} and excited state {ES} structures. (a) Results for sets of 44 GS and 1100 ES structures in the time range $2.0\,\text{ps} < t < 2.03\,\text{ps}$ from BOMD trajectories. (b) Results for the same set of BOMD structures as in (a), but with constrained Ir-Ir distances. (c,d) Results for two sets of DFT structures, where the Ir-Ir bond in GS and ES structures was varied according to the Gaussian distribution with (c) $\sigma_{\text{Ir-Ir}} = 0.1\,\text{Å}$ and (d) $\sigma_{\text{Ir-Ir}} = 0.2\,\text{Å}$ (see the text for details). The dotted lines in (a)-(c) along the direction $q_1 = q_2$ define the sections through the maps for $n=0$, which produce four curves of the corresponding colors in Fig. 11(d).

packet shape.

At the same time, the agreement between our experiment and simulations is not perfect, and is most likely limited by the accuracy of the constructed sample models. A more rigorous quantitative comparison would require more advanced models, particularly to accommodate solvent effects, which are considered to be an important component accompanying chemical reactions in solutions [35,61,67,80]. Our trial simulations with solvated $[\text{Ir}_2(\text{dimen})_4]^{2+}$ molecules (see see Section S6 of the ESI†) indicate that solvent effects can potentially also be analyzed using the correlation approach. Therefore, it is expected that also more complex effects contributing to photoexcited dynamics in molecular ensembles can be studied using the proposed approach, provided that sufficiently accurate sample models can be constructed.

Author Contributions

KH, IAV, MMN designed the experiment. KSP prepared the experimental samples. TBD, AOD, IAZ, NM, DBZ, MS, GIR, EB, KH, MMN carried out the experiment and collected the data. TBD, SN performed initial data reduction. RPK performed correlation analysis of the data. AOD, RPK performed simulations. TBB, RPK, IAV performed theoretical analysis of the cross-correlation functions. RPK wrote the manuscript with the input from all coauthors. All authors contributed to the discussion of the experimental and simulation results, and carefully revised the manuscript.

Conflicts of interest

There are no conflicts to declare.

Acknowledgements

Notes and references

1 Q. Liu, J. Wang and A. H. Zewail, *Nature*, 1993, **364**, 427–430.

2 W. Zhang, R. Alonso-Mori, U. Bergmann, C. Bressler, M. Chollet, A. Galler, W. Gawelda, R. G. Hadt, R. W. Hartsock, T. Kroll,

K. S. Kjær, K. Kubiček, H. T. Lemke, H. W. Liang, D. A. Meyer, M. M. Nielsen, C. Purser, J. S. Robinson, E. I. Solomon, Z. Sun, D. Sokaras, T. B. van Driel, G. Vankó, T.-C. Weng, D. Zhu and K. J. Gaffney, *Nature*, 2014, **509**, 345–348.

3   S. E. Canton, K. S. Kjær, G. Vankó, T. B. van Driel, S. Adachi, A. Bordage, C. Bressler, P. Chabera, M. Christensen, A. O. Dohn, A. Galler, W. Gawelda, D. Gosztola, K. Haldrup, T. Harlang, Y. Liu, K. B. Møller, Z. Németh, S. Nozawa, M. Pápai, T. Sato, T. Sato, K. Suarez-Alcantara, T. Togashi, K. Tono, J. Uhlig, D. A. Vithanage, K. Wärnmark, M. Yabashi, J. Zhang, V. Sundström and M. M. Nielsen, *Nature Communications*, 2015, **6**, 6359.

4   K. H. Kim, J. G. Kim, S. Nozawa, T. Sato, K. Y. Oang, T. W. Kim, H. Ki, J. Jo, S. Park, C. Song, T. Sato, K. Ogawa, T. Togashi, K. Tono, M. Yabashi, T. Ishikawa, J. Kim, R. Ryoo, J. Kim, H.Ihee and S. Adachi, *Nature*, 2015, **518**, 385.

5   J. M. Glownia, A. Natan, J. P. Cryan, R. Hartsock, M. Kozina, M. P. Minitti, S. Nelson, J. Robinson, T. Sato, T. B. van Driel, G. Welch, C. Weninger, D. Zhu and P. Bucksbaum, *Phys. Rev. Lett.*, 2016, **117**, 153003.

6   D. Khakhulin, L. M. Lawson-Daku, D. Leshchev, G. E. Newby, M. Jarenmark, C. Bressler, M. Wulff and S. E. Canton, *Phys. Chem. Chem. Phys.*, 2019, **21**, 9277–9284.

7   B. Stankus, H. Yong, N. Zotev, J. M. Ruddock, D. Bellshaw, T. J. Lane, M. Liang, S. Boutet, S. Carbajo, J. S. Robinson, W. Du, N. Goff, Y. Chang, J. E. Koglin, M. P. Minitti, A. Kirrander and P. M. Weber, *Nature chemistry*, 2019, **11**, 716–721.

8   J. Yang, X. Zhu, J. P. F. Nunes, J. K. Yu, R. M. Parrish, T. J. A. Wolf, M. Centurion, M. Gühr, R. Li, Y. Liu, B. Moore, M. Niebuhr, S. Park, X. Shen, S. Weathersby, T. Weinacht, T. J. Martinez and X. Wang, *Science*, 2020, **368**, 885–889.

9   H. Ihee, *Accounts of Chemical Research*, 2009, **42**, 356–366.

10 T. K. Kim, J. H. Lee, M. Wulff, Q. Kong and H. Ihee, *ChemPhysChem*, 2009, **10**, 1958–1980.

11 C. Bressler, C. Milne, V.-T. Pham, A. Elnahhas, R. M. van der Veen, W. Gawelda, S. Johnson, P. Beaud, D. Grolimund, M. Kaiser, C. N. Borca, G. Ingold, R. Abela and M. Chergui, *Science*, 2009, **323**, 489–492.

12 K. Haldrup, G. Vankó, W. Gawelda, A. Galler, G. Doumy, A. M. March, E. P. Kanter, A. Bordage, A. Dohn, T. B. van Driel, K. S. Kjær, H. T. Lemke, S. E. Canton, J. Uhlig, V. Sundström, L. Young, S. H. Southworth, M. M. Nielsen and C. Bressler, *J. Phys. Chem. A*, 2012, **116**, 9878–9887.

13 M. Chergui, *Acc. Chem. Res.*, 2015, **48**, 801–808.

14 L. X. Chen, *X-Ray Absorption and X-Ray Emission Spectroscopy: Theory and Applications*, Wiley, 2015, vol. 1, ch. 9, pp. 213–250.

15 A. S. Rury, T. E. Wiley and R. J. Sension, *Acc. Chem. Res.*, 2015, **48**, 860–867.

16 M. P. Minitti, J. M. Budarz, A. Kirrander, J. S. Robinson, D. Ratner, T. J. Lane, D. Zhu, J. M. Glownia, M. Kozina, H. T. Lemke, M. Sikorski, Y. Feng, S. Nelson, K. Saita, B. Stankus, T. Northey, J. B. Hastings and P. M. Weber, *Phys. Rev. Lett.*, 2015, **114**, 255501.

17 A. R. Attar, A. Bhattacherjee, C. D. Pemmaraju, K. Schnorr, K. D. Closser, D. Prendergast and S. R. Leone, *Science*, 2017, **356**, 54–59.

18 N. A. Miller, A. Deb, R. Alonso-Mori, J. M. Glownia, L. M. Kiefer, A. Konar, L. B. Michocki, M. Sikorski, D. L. Sofferman, S. Song, M. J. Toda, T. E. Wiley, D. Zhu, P. M. Kozlowski, K. J. Kubarych, J. E. Penner-Hahn and R. J. Sension, *J. Phys. Chem. A*, 2018, **122**, 4963–4971.

19 K. S. Kjær, N. Kaul, O. Prakash, P. Chábera, N. W. Rosemann, A. Honarfar, O. Gordivska, L. A. Fredin, K.-E. Bergquist, L. Häggström, T. Ericsson, L. Lindh, A. Yartsev, S. Styring, P. Huang, J. Uhlig, J. Bendix, D. Strand, V. Sundström, P. Persson, R. Lomoth and K. Wärnmark, *Science*, 2019, **363**, 249–253.

20 D. Kinschel, C. Bacellar, O. Cannelli, B. Sorokin, T. Katayama, G. F. Mancini, J. R. Rouxel, Y. Obara, J. Nishitani, H. Ito, T. Ito, N. Kurahashi, C. Higashimura, S. Kudo, T. Keane, F. A. Lima, W. Gawelda, P. Zalden, S. Schulz, J. M. Budarz, D. Khakhulin, A. Galler, C. Bressler, C. J. Milne, T. Penfold, M. Yabashi, T. Suzuki, K. Misawa and M. Chergui, *Nature Communications*, 2020, **11**, 4145.

21 S. Asban, D. Cho and S. Mukamel, *J. Phys. Chem. Lett.*, 2019, **10**, 5805–5814.

22 S. M. Cavaletto, D. Keefer, J. R. Rouxel, F. Aleotti, F. Segatta, M. Garavelli and S. Mukamel, *Proc. Nat. Acad. Sci.*, 2021, **118**, e2105046118.

23 K. J. Gaffney and H. N. Chapman, *Science*, 2007, **316**, 1444–1448.

24 M. Cammarata, M. Levantino, F. Schotte, P. A. Anfinrud, F. Ewald, J. Choi, A. Cupane, M. Wulff and H. Ihee, *Nature Methods*, 2008, **5**, 881–886.

25 H. T. Lemke, C. Bressler, L. X. Chen, D. M. Fritz, K. J. Gaffney, A. Galler, W. Gawelda, K. Haldrup, R. W. Hartsock, H. Ihee, J. Kim, K. H. Kim, J. H. Lee, M. M. Nielsen, A. B. Stickrath, W. Zhang, D. Zhu and M. Cammarata, *J. Phys. Chem. A*, 2013, **117**, 735–740.

26 M. Chergui and E. Collet, *Chem. Rev.*, 2017, **117**, 11025–11065.

27 L. X. Chen, *X-Ray Free Electron Lasers: Applications in Materials, Chemistry and Biology*, Royal Chem. Soc. Publishing, 2017, ch. 10, pp. 201–224.

28 E. Collet and M. Cammarata, *Chem. Eur. J.*, 2018, **24**, 15696–15705.

29 E. Biasin, T. B. van Driel, K. S. Kjær, A. O. Dohn, M. Christensen, T. Harlang, P. Chabera, Y. Liu, J. Uhlig, M. Pápai, Z. Németh, R. Hartsock, W. Liang, J. Zhang, R. Alonso-Mori, M. Chollet, J. M. Glownia, S. Nelson, D. Sokaras, T. A. Assefa, A. Britz, A. Galler, W. Gawelda, C. Bressler, K. J. Gaffney, H. Lemke, K. B. Møller, M. M. Nielsen, V. Sundström, G. Vankó, K. Wärnmark, S. E. Canton and K. Haldrup, *Phys. Rev. Lett.*, 2016, **117**, 013002.

30 K. Kunnus, M. Vacher, T. C. B. Harlang, K. S. Kjær, K. Haldrup, E. Biasin, T. B. van Driel, M. Pápai, P. Chabera, Y. Liu, H. Tatsuno, C. Timm, E. Källman, M. Delcey, R. W. Hartsock, M. E. Reinhard, S. Koroidov, M. G. Laursen, F. B. Hansen, P. Vester,

M. Christensen, L. Sandberg, Z. Németh, D. S. Szemes, É. Bajnóczi, R. Alonso-Mori, J. M. Glownia, S. Nelson, M. Sikorski, D. Sokaras, H. T. Lemke, S. E. Canton, K. B. Møller, M. M. Nielsen, G. Vankó, K. Wärnmark, V. Sundström, P. Persson, M. Lundberg, J. Uhlig and K. J. Gaffney, *Nature Communications*, 2020, **11**, 634.

31 H. Yong, N. Zotev, J. M. Ruddock, B. Stankus, M. Simmermacher, A. M. Carrascosa, W. Du, N. Goff, Y. Chang, D. Bellshaw, M. Liang, S. Carbajo, J. E. Koglin, J. S. Robinson, S. Boutet, M. P. Minitti, A. Kirrander and P. M. Weber, *Nature Communications*, 2020, **11**, 2157.

32 J. G. Kim, S. Nozawa, H. Kim, E. H. Choi, T. Sato, T. W. Kim, K. H. Kim, H. Ki, J. Kim, M. Choi, Y. Lee, J. Heo, K. Y. Oang, K. Ichiyanagi, R. Fukaya, J. H. Lee, J. Park, I. Eom, S. H. Chun, S. Kim, M. Kim, T. Katayama, T. Togashi, S. Owada, M. Yabashi, S. J. Lee, S. Lee, C. W. Ahn, D.-S. Ahn, J. Moon, S. Choi, J. Kim, T. Joo, J. Kim, S. Adachi and H. Ihee, *Nature*, 2020, **582**, 520–524.

33 M. R. Panman, E. Biasin, O. Berntsson, M. Hermann, S. Niebling, A. J. Hughes, J. Kübel, K. Atkovska, E. Gustavsson, A. Nimmrich, A. O. Dohn, M. Laursen, D. B. Zederkof, A. Honarfar, K. Tono, T. Katayama, S. Owada, T. B. van Driel, K. Kjær, M. M. Nielsen, J. Davidsson, J. Uhlig, K. Haldrup, J. S. Hub and S. Westenhoff, *Phys. Rev. Lett.*, 2020, **125**, 226001.

34 M. E. Reinhard, M. W. Mara, T. Kroll, H. Lim, R. G. Hadt, R. Alonso-Mori, M. Chollet, J. M. Glownia, S. Nelson, D. Sokaras, K. Kunnus, T. B. van Driel, R. W. Hartsock, K. S. Kjær, C. Weninger, E. Biasin, L. B. Gee, K. O. Hodgson, B. Hedman, U. Bergmann, E. I. Solomon and K. J. Gaffney, *Nature Communications*, 2021, **12**, 1086.

35 E. Biasin, Z. W. Fox, A. Andersen, K. Ledbetter, K. S. Kjær, R. Alonso-Mori, J. M. Carlstad, M. Chollet, J. D. Gaynor, J. M. Glownia, K. Hong, T. Kroll, J. H. Lee, C. Liekhus-Schmaltz, M. Reinhard, D. Sokaras, Y. Zhang, G. Doumy, A. M. March, S. H. Southworth, S. Mukamel, K. J. Gaffney, R. W. Schoenlein, N. Govind, A. A. Cordones and M. Khalil, *Nature Chemistry*, 2021, **13**, 343–349.

36 E. H. Choi, Y. Lee, J. Heo and H. Ihee, *Chem. Sci.*, 2022, **13**, 8457–8490.

37 D. A. Kohl and E. J. Shipsey, *Z. Phys. D - Atoms, Molecules and Clusters*, 1992, **24**, 33–38.

38 J. C. Williamson and A. H. Zewail, *J. Phys. Chem.*, 1994, **98**, 2766–2781.

39 M. Ben-Nun, J. Cao and K. Wilson, *The Journal of Physical Chemistry A*, 1997, **101**, 8743–8761.

40 J. S. Baskin and A. H. Zewail, *ChemPhysChem*, 2005, **6**, 2261–2276.

41 J. S. Baskin and A. H. Zewail, *ChemPhysChem*, 2006, **7**, 1562–1574.

42 K. Hoshina, K. Yamanouchi, T. Ohshima, Y. Ose and H. Todokoro, *J. Chem. Phys.*, 2003, **118**, 6211–6221.

43 P. Reckenthaeler, M. Centurion, W. Fuss, S. A. Trushin, F. Krausz and E. E. Fill, *Phys. Rev. Lett.*, 2009, **102**, 213001.

44 C. J. Hensley, J. Yang and M. Centurion, *Phys. Rev. Lett.*, 2012, **109**, 133202.

45 U. Lorenz, K. B. Møller and N. E. Henriksen, *New J. Phys.*, 2010, **12**, 113022.

46 T. J. Penfold, I. Tavernelli, R. Abela, M. Chergui and U. Rothlisberger, *New J. Phys.*, 2012, **14**, 113002.

47 E. Biasin, T. B. van Driel, G. Levi, M. G. Laursen, A. O. Dohn, A. Moltke, P. Vester, F. B. K. Hansen, K. S. Kjær, T. Harlang, R. Hartsock, M. Christensen, K. J. Gaffney, N. E. Henriksen, K. B. Møller, K. Haldrup and M. M. Nielsen, *J. Synchrotron Rad.*, 2018, **25**, 306–315.

48 K. Haldrup, G. Levi, E. Biasin, P. Vester, M. G. Laursen, F. Beyer, K. S. Kjær, T. B. van Driel, T. Harlang, A. O. Dohn, R. J. Hartsock, S. Nelson, J. M. Glownia, H. T. Lemke, M. Christensen, K. J. Gaffney, N. E. Henriksen, K. B. Møller and M. M. Nielsen, *Phys. Rev. Lett.*, 2019, **122**, 063001.

49 A. Natan, A. Schori, G. Owolabi, J. P. Cryan, J. M. Glownia and P. H. Bucksbaum, *Faraday Discussions*, 2021, **228**, 123–138.

50 M. Altarelli, R. P. Kurta and I. A. Vartanyants, *Phys. Rev. B*, 2010, **82**, 104207.

51 R. P. Kurta, M. Altarelli and I. A. Vartanyants, *Advances in Condensed Matter Physics*, 2013, **2013**, 959835.

52 R. P. Kurta, M. Altarelli and I. A. Vartanyants, *Advances in Chemical Physics*, 2016, **161**, 1–39.

53 Z. Kam, *Macromolecules*, 1977, **10**, 927–934.

54 R. P. Kurta, J. J. Donatelli, C. H. Yoon, P. Berntsen, J. Bielecki, B. J. Daurer, H. DeMirci, P. Fromme, M. F. Hantke, F. R. N. C. Maia, A. Munke, C. Nettelblad, K. Pande, H. K. N. Reddy, J. A. Sellberg, R. G. Sierra, M. Svenda, G. van der Schot, I. A. Vartanyants, G. J. Williams, P. L. Xavier, A. Aquila, P. H. Zwart and A. P. Mancuso, *Phys. Rev. Lett.*, 2017, **119**, 158102.

55 K. Pande, J. J. Donatelli, E. Malmerberg, L. Foucar, C. Bostedt, I. Schlichting and P. H. Zwart, *Proc. Nat. Acad. Sci. USA*, 2018, **115**, 11772–11777.

56 R. P. Kurta, B. I. Ostrovskii, A. Singer, O. Y. Gorobtsov, A. Shabalin, D. Dzhigaev, O. M. Yefanov, A. V. Zozulya, M. Sprung and I. A. Vartanyants, *Phys. Rev. E*, 2013, **88**, 044501.

57 I. A. Zaluzhnyy, R. P. Kurta, E. A. Sulyanova, O. Y. Gorobtsov, A. G. Shabalin, A. V. Zozulya, A. P. Menushenkov, M. Sprung, A. Krówczyński, E. Górecka, B. I. Ostrovskii and I. A. Vartanyants, *Soft Matter*, 2017, **13**, 3240.

58 R. P. Kurta, L. Wiegart, A. Fluerasu and A. Madsen, *IUCrJ*, 2019, **16**, 635–648.

59 J. Binns, C. Darmanin, C. M. Kewish, S. K. Pathirannahalge, P. Berntsen, P. L. R. Adams, S. Paporakis, D. Wells, F. G. Roque, B. Abbey, G. Bryant, C. E. Conn, S. T. Mudie, A. M. Hawley, T. M. Ryan, T. L. Greaves and A. V. Martin, *IUCRj*, 2022, **9**, 231–242.

60 P. Vester, I. A. Zaluzhnyy, R. P. Kurta, K. B. Møller, E. Biasin, K. Haldrup, M. M. Nielsen and I. A. Vartanyants, *Structural Dynamics*, 2019, **6**, 024301.

61 A. O. Dohn, E. Ö. Jónsson, K. S. Kjær, T. B. van Driel, M. M. Nielsen, K. W. Jacobsen, N. E. Henriksen and K. B. Møller, *J. Phys. Chem. Lett.*, 2014, **5**, 2414–2418.

62 H. B. Gray, S. Záliš and A. Vlček, *Coord. Chem. Rev.*, 2017,

345, 297–317.

63 C. L. Exstrom, D. Britton, K. R. Mann, M. G. Hill, V. M. Miskowski, W. P. Schaefer, H. B. Gray and W. M. Lamanna, *Inorg. Chem.*, 1996, **35**, 549–550.

64 K. Haldrup, T. Harlang, M. Christensen, A. Dohn, T. B. van Driel, K. S. Kjær, N. Harrit, J. Vibenholt, L. Guerin, M. Wulff and M. M. Nielsen, *Inorganic Chemistry*, 2011, **50**, 9329–9336.

65 R. W. Hartsock, W. Zhang, M. G. Hill, B. Sabat and K. J. Gaffney, *J. Phys. Chem. A*, 2011, **115**, 2920–2926.

66 M. Pižl, B. M. Hunter, I. V. Sazanovich, M. Towrie, H. B. Gray, S. Záliš and A. Vlček, *Inorg. Chem.*, 2022, **61**, 2745–2759.

67 T. B. van Driel, K. S. Kjær, R. W. Hartsock, A. O. Dohn, T. Harlang, M.Chollet, M. Christensen, W. Gawelda, N. E. Henriksen, J. G. Kim, K. Haldrup, K. H. Kim, H. Ihee, J. Kim, H. Lemke, Z. Sun, V. Sundström, W. Zhang, D. Zhu, K. B. Møller, M. M. Nielsen and K. J. Gaffney, *Nature Communications*, 2016, **7**, 13678.

68 V. M. Minkowski, T. P. Smith, T. M. Loehr and H. B. Gray, *J. Am. Chem. Soc.*, 1985, **107**, 7925–7934.

69 R. Alonso-Mori, C. Caronna, M. Chollet, R. Curtis, D. S. Damiani, J. Defever, Y. Feng, D. L. Flath, J. M. Glownia, S. Lee, H. T. Lemke, S. Nelson, E. Bong, M. Sikorski, S. Song, V. Srinivasan, D. Stefanescu, D. Zhu and A. Robert, *J. Synchrotron Rad.*, 2015, **22**, 508–513.

70 G. Blaj, A. Dragone, C. J. Kenney, F. Abu-Nimeh, P. Caragiulo, D.Doering, M. Kwiatkowski, B. Markovic, J. J. Pines, M. Weaver, S. Boutet, G. Carini, C.-E. Chang, P. Hart, J. Hasi, M. Hayes, R. Herbst, J. Koglin, K. Nakahara, J. Segal and G. Haller, *AIP Conf. Proc.*, 2019, **2054**, 060062.

71 A. Montoya-Castillo, M. S. Chen, S. L. Raj, K. A. Jung, K. S. Kjaer, T. Morawietz, K. J. Gaffney, T. B. van Driel and T. E. Markland, *Phys. Rev. Lett.*, 2022, **129**, 056001.

72 K. Haldrup, M. Christensen and M. M. Nielsen, *Acta Cryst.*, 2010, **A66**, 261–269.

73 S. Palese, L. Schilling, R. J. D. Miller, P. R. Staver and W. T. Lotshaw, *J. Phys. Chem.*, 1994, **98**, 6308–6316.

74 R. Jimenez, G. R. Fleming, P. V. Kumar and M. Maroncelli, *Nature*, 1994, **369**, 471.

75 E. W. Castner, Y. J. Chang, Y. C. Chu and G. E.Walrafen, *J. Chem. Phys.*, 1995, **102**, 653–659.

76 H. Ki, S. Choi, J. Kim, E. H. Choi, S. Lee, Y. Lee, K. Yoon, C. W. Ahn, D.-S. Ahn, J. H. Lee, J. Park, I. Eom, M. Kim, S. H. Chun, J. Kim, H. Ihee and J. Kim, *J. Am. Chem. Soc.*, 2021, **143**, 14261–14273.

77 H. Yong, N. Zotev, B. Stankus, J. M. Ruddock, D. Bellshaw, S. Boutet, T. J. Lane, M. Liang, S. Carbajo, J. S. Robinson, W. Du, N. Goff, Y. Chang, J. E. Koglin, M. D. J. Waters, T. I. Sølling, M. P. Minitti, A. Kirrander and P. M. Weber, *J. Phys. Chem. Lett.*, 2018, **9**, 6556–6562.

78 B. M. Hunter, R. M. Villahermosa, C. L. Exstrom, M. G. Hill, K. R. Mann and H. B. Gray, *Inorganic chemistry*, 2012, **51**, 6898–6905.

79 B. Nordén, *Applied Spectroscopy Reviews*, 1978, **14**, 157–248.

80 P. Vester, K. Kubicek, R. Alonso-Mori, T. Assefa, E. Biasin, M. Christensen, A. O. Dohn, T. B. van Driel, A. Galler, W. Gawelda, T. C. B. Harlang, N. E. Henriksen, K. S. Kjær, T. S. Kuhlman, Z. Németh, Z. Nurekeyev, M. Pápai, J. Rittman, G. Vankó, H. Yavas, D. B. Zederkof, U. Bergmann, M. M. Nielsen, K. B. Møller, K. Haldrup and C. Bressler, *J. Chem. Phys.*, 2022, **157**, 224201.